

# Aerothermal Optimization of Film Cooling Hole Locations on the Squealer Tip of an HP Turbine Blade

F. Yıldız<sup>a</sup>, E. Alpman<sup>b</sup>, L. Kavurmacioğlu<sup>a</sup>, C. Camcı<sup>c</sup>

<sup>a</sup>*Istanbul Technical University, Dept. of Mechanical Eng., 34437 Istanbul, Turkey*

<sup>b</sup>*Marmara University, Mechanical Eng. Dept., Göztepe Campus, 34722 Istanbul, Turkey*

<sup>c</sup>*Fellow ASME, The Pennsylvania State University, Dept. of Aerospace Engineering Turbomachinery Aero-Heat Transfer Lab, University Park, PA, 16802, USA*

---

## Abstract

This paper presents a time-efficient method to optimize the positions of film cooling holes on a gas turbine blade's squealer tip for cooling and aerodynamic performance. A computational approach is employed for the optimization, including validations against experiments. Five discrete film cooling holes are considered, and two different blowing ratios of 0.4 and 1.0 are studied. The positions of cooling holes on the tip along the tangential direction are varied as the input parameters of optimization. The multi-objective optimization uses an algorithm with an artificial neural network for fast fitness function predictions. The best cooling configuration found by the optimization achieves a 13.43% reduction in total heat flux and a 0.4% increase in aerodynamic loss when the blowing rate is 1.0. Including the casing relative motion in the computations results in a total pressure loss coefficient increase of about 8 % for both blowing ratios. For  $M=1.0$ , imposing the casing's motion results in a 10.2% reduction in total heat transfer to the tip compared to the stationary casing. For the lower blowing rate of 0.4, the total heat flux reduction to the tip is 12.0% because of imposed casing motion. Hence, the cooling effectiveness can be improved by employing the particular position optimization method presented in this study. The results suggest that experimental and computational heat transfer studies on cooled turbine blade tips, especially in cascade arrangements, need to consider the relative motion of the blade tip.

**Keywords:** Turbine, Film cooling, Squealer blade tip, Blowing ratio, Casing relative motion, Multi-objective optimization

---

## Nomenclature

### Latin Symbols

$\Delta C_{p0}$	Change of $C_{p0}$
$C$	Chord
$C_{p0}$	Total pressure coefficient
$C_p$	Static pressure coefficient
$c_p$	Specific heat capacity
$C_x$	Axial chord
$d$	Film cooling hole diameter
$h$	Blade height
$h$	Convective heat transfer coefficient
$\dot{m}$	Mass flow rate
$M$	Blowing ratio ( $M = \rho_c U_c / \rho_\infty U_\infty$ )
$p$	Pressure
$p_0$	Mass averaged total pressure at the inlet
$p_{0i}$	Mass averaged total pressure at the inlet
$p_i$	Inlet static pressure
$Pr$	Laminar Prandtl number
$Pr_t$	Turbulent Prandtl number
$q''_w$	Wall heat flux
$q_{cavity}$	Heat transfer rate on the cavity surface
$q_{side}$	Heat transfer rate on the inside of the squealer rim
$q_{tip}$	Heat transfer rate on top of the squealer rim
$S$	Blade pitch
$s$	Squealer height
$T$	Temperature
$t$	Tip clearance
$T_{0\infty}$	Free stream total temperature
$T_{0c}$	Coolant total temperature
$T_{0i}$	Mass flow averaged temperature at the inlet
$T_w$	Wall temperature
$U_\infty$	Mainstream velocity
$U_c$	Coolant velocity
$U_i$	Inlet velocity
$U_m$	Blade velocity at mid-span of AFTRF test blade (63.5 m/s)
$w$	Squealer width
$x$	Axial direction, measured from the leading edge
$y$	Tangential direction
$Y_i$	Actual testing data
$\hat{Y}_i$	Network predictions

### Greek Symbols

$\alpha$	Inlet flow angle
$\Gamma$	$\frac{q_{total,actual} - q_{total,reference}}{q_{total,reference}}$
$\delta C_p / C_p$	Uncertainty of static pressure coefficient
$\delta h / h$	Uncertainty of heat transfer coefficient
$\kappa_{eff}$	Effective heat conductivity
$\kappa_t$	Turbulent heat conductivity
$\nu$	Kinematic viscosity
$\nu_t$	Turbulent viscosity
$\rho$	Density
$\rho_\infty$	Mainstream density
$\rho_c$	Coolant density
$\omega$	Specific rate of dissipation
$\Omega$	$\frac{\Delta C_{p0,actual} - \Delta C_{p0,reference}}{\Delta C_{p0,reference}}$

### Abbreviations

AFTRF	Axial flow turbine research facility
ANN	Artificial neural network
CFD	Computational fluid dynamics
ELM	Extreme Learning Machine
FC	Film cooling
FFNN	Feed-forward neural network
MSE	Mean square error
NSGA – II	Nondominated sorting genetic algorithm
PS	Pressure side
RANS	Reynolds-averaged Navier-Stokes
RM	Casing relative motion
SVM	Support Vector Machine

SS	Suction side
SST	Shear stress transport

### Subscript

$\infty$	Free stream
$i$	Inlet
$c$	Coolant

## 1. Introduction

The thermal efficiency of gas turbine engines has become increasingly critical over the years for better fuel efficiency and improved specific power. Temperatures of the first-stage turbine inlets easily exceed 1300 °C [1]. High thermal loads frequently occur on turbine blades and create durability problems. As a result, the cooling of turbine blades is a must, and film cooling is the preferred external cooling method for a turbine blade. Unlike internal cooling, external cooling decreases the convective heat transfer rate to protect the blade surface from melting and local oxidation damage. **Especially for unshrouded blades, cooling the blade tip becomes more complicated, with tip leakage flow occurring because of the strong pressure differentials between the pressure side and the suction side. Tip leakage flow measurably reduces the aerodynamic efficiency and hinders the cooling effectiveness of the blade tip.** Thus, many studies focus on tip designs and film cooling to protect the tip region, aiming to reduce leakage flow and convective heat transfer rate.

***Various tip leakage mitigation schemes:*** The rate of tip leakage loss is related to many different parameters. The gap height between the tip surface and the stationary shroud is one of them, and tip leakage flow decreases with decreasing gap height because of the viscosity effect. Saha et al. [2] mentioned that tip gap height can be reduced by using a squealer tip design. A squealer tip design allows an uninterrupted turbine operation in a potential rubbing incident between the blade and the casing. The only damage is generally to the squealer cavity rims, and the tip cooling system remains intact. In addition, a separation vortex occurs near the pressure side rim of the squealer cavity and creates resistance to leakage loss. It acts as a labyrinth seal [3]. Tip clearance also affects cooling performance on the tip region as the leakage mass flow rate varies. Acharya et al. [4] showed that film cooling effectiveness increases with decreasing clearance as leakage mass flow is reduced.

Altering the conventional tip platform design could significantly reduce tip leakage loss. The squealer tip design is one of the most popular strategies to date. Key and Arts [5] studied a squealer tip and showed that their design significantly reduced tip leakage compared to a flat tip. Like this research, Schabowski et al. [6] have compared winglet and plane tip designs and reported that the winglet tip decreases aerodynamic loss. Dey and Cameci [7] studied several winglet tip designs in the rotating turbine rig 'Axial Flow Turbine Research Facility' (AFTRF). They compared PS and SS tip extensions against a baseline tip and showed that PS tip extension significantly decreased tip leakage-related aerodynamic loss. Ledezma et al. [8] have investigated the impact of different tip designs on tip leakage flow. They showed a squealer tip design without a pressure side rim, and a pressure side winglet design has higher total exit pressure than the conventional squealer tip design.

***Influence of tip desensitization on heat transfer:*** Besides increasing aerodynamic performance, tip

desensitization decreases the heat transfer rate at the tip surface because of the tip leakage flow's reduced mass flow rate. Yan et al. [9] investigated the influences of winglet and squealer tips on heat transfer and leakage loss. Besides, the impact of the multi-cavity tip on the aerothermal performance of turbine blades has been studied by Du et al. [10]. They showed that the single-cavity tip performs better than their divided multi-cavity tip design and plane tip case. Jiang et al. [11] researched the impact of squealer tip design with winglets on turbine aerothermal performance using three different tip designs. They demonstrated performance improvements when compared to conventional squealer tip design. Unlike these investigations, Zhou et al. [12] presented that blade tip coolant injection could effectively reduce cavity floor heat load. However, its effect on the casing is less pronounced. They also showed that simultaneous tip film cooling and casing purge cooling could effectively reduce the casing and cavity floor's heat load. Yan et al. [13] investigated the addition of multiple ribs onto the squealer tip cavity's bottom surface to weaken the cavity vortex and increase the efficiency of film cooling. They studied multiple rib arrangements of straight ribs, V-shape ribs, and L-shaped ribs. L-shape rib design showed the best performance in cooling the tip region.

***Tip leakage mitigation and film cooling:*** Film cooling can also change the tip flow characteristic at the tip gap. Complex viscous flow in the tip gap is critical, especially for aerodynamically optimized tip designs. Wang et al. [14] have shown that leakage flow near the leading edge decreases with film cooling compared to without film cooling case. Sakaoglu and Kahveci [15] investigated the combined effects of film cooling and rotation on tip gap flow characteristics. They reported that the heat transfer is reduced on the tip surface with the impact of rotation for both cooled and uncooled cases, and rotation also presses the high heat transfer zone to the pressure side of the cavity. They also showed the impact of cavity depth on the film cooling performance. They pointed out that increasing the cavity depth reduces the average heat transfer coefficient above the depth-to-width ratio of 1.5.

Tip leakage flow contains vortices and a complex structure that tries to pull the film cooling layer from the tip surface. In this situation, the film layer cannot protect the tip surface effectively. The solution to this problem is to use angled and shaped cooling holes. Eriksen and Goldstein [16] investigated the impact of various angled film cooling holes and presented that 35° angled holes show better cooling performance than a normal injection. Yan et al. [17] also researched that subject with different injection angles in pitchwise and streamwise directions. Kim and Metzger [18] studied slot-shaped film cooling holes close to the pressure side of the tip region. They reported a good performance, especially for the spanwise direction where the holes were located. Cunliang et al. [19] presented an experimental study to show the effect of laid-back fan-shaped holes on the rim surface. They

used cylindrical holes for comparison and reported that laid-back fan-shaped holes are better than cylindrical holes in rim protection, even if the same compound angle is used. Wang et al. [20] studied the optimization of fan-shaped holes on a flat surface. They used inclination angle, lateral expansion angle and hole length as input parameters and reported the optimized designs for different blowing ratios in a range between  $M=0.5$  and  $M=1.5$ . On the other hand, Zhang et al. [21] investigated the tangential jets cooling on a divided squealer tip. They pointed out the tangential jet coolant almost covers the cavity surface downstream.

***Influence of blowing rate on film cooling performance:*** The blowing ratio is another crucial variable that changes cooling performance because coolant flow should have enough energy to surpass tip flow and create a proper coolant layer on the tip surface. Many studies focused on this subject and showed that increasing the blowing ratio increases the cooling performance [22, 23, 24] up to a specific value. Over that optimal value, the film cooling jet penetrates the free stream and loses its cooling effectiveness. An unnecessarily high blowing ratio also reduces the turbine efficiency by consuming too much-pressurized air from the cycle. The present study used a blowing rate of 1.0 and 0.4 to investigate the influence of high and low coolant momentum flux rates over a film-cooled squealer cavity.

In addition to hole shape, injection angle, and blowing rate, the number and positions of holes significantly affect film cooling effectiveness and tip leakage flow characteristics. Rao and Camci [25] presented a tip injection study in the rotating turbine research rig (AFTRF). They observed that different injection locations have a measurable impact on the development of leakage vortex. Phase-locked and time-accurate total pressure surveys obtained downstream of the rotor of the AFTRF documented the impact of the tip cooling injection on the tip leakage flow structure. Cheng et al. [26] studied camber line and suction side holes with changing numbers and showed that film cooling protection increased with an increasing number of holes and cooling of the blade tip leading edge was more challenging than in the other zones. Another numerical study of film hole arrangements was reported by Yang et al. [27]. They used three different hole arrangements. The first one is the camber arrangement in which the film cooling holes are placed on the camber line. The second arrangement places the film cooling holes close to the suction side. Their final arrangement was a two-row configuration in which the film cooling holes were placed on the camber line. The two-row arrangement performed better than the camber line arrangement, especially for the higher blowing ratios. Ahn et al. [28] studied film cooling with tip holes placed on the camber line, holes on the pressure side, and holes on the tip and the pressure side on a squealer tip geometry. Only the holes on the camber line arrangement effectively cooled the cavity floor. Comparing the hole arrangements on the tip and the pressure side showed that the impact of pressure side holes

on cooling performance is negligible for the squealer tip design. He [29] investigated a squealer tip configuration with cavity camberline holes and pressure side holes. He showed that only the cavity camberline holes on the tip could effectively cool the cavity floor. **Tong et al. also studied different film cooling hole arrangements [30]. They reported that a denser hole distribution near the leading edge provides better cooling performance.**

Park et al. [31] showed that the suction side case had the worst cooling effectiveness. His investigation included the effects of different hole arrangements, such as single-row cooling holes along the camber line near the pressure and suction side rim. They found better film cooling effectiveness when the holes were near the pressure side and inclined to the suction side from the leading edge to the trailing edge. Unlike these studies, Wang et al. [32] investigated the importance of injection position in a honeycomb tip using a turbine cascade. They showed that injection orientation and position changes affect the cooling and tip leakage flow.

***An outline of the current optimization approach for tip film cooling in a squealer cavity:*** Previous studies showed that the locations of film cooling holes significantly affect film cooling effectiveness. Moreover, film cooling can also strongly affect the tip flow structure and change the overall aerodynamic performance of the blade. **Considering these observations, a conventional and uncooled squealer blade tip design with a relatively low aerodynamic loss but high heat transfer on the tip region was selected for an aerothermal optimization study.** Details of this specific optimization strategy without tip cooling were reported by Senel et al. in [33]. The current research extends the specific optimization approach of [33] to a film-cooled squealer tip geometry. Most past studies for a film-cooled tip are with a stationary casing, mainly in linear cascade configurations. This investigation shows that the inclusion of the relative motion of the casing has a strong positive influence on the heat transfer rates. This study aims to reduce the heat transfer on the tip surface with controlled aerodynamic loss by optimizing the positions of the film cooling holes. For this purpose, five discrete film cooling holes are used, and four of them are optimized in the blade's tangential direction (y-direction), as shown in Figure 1. The fifth hole's position, which is close to the trailing edge, is fixed. Its impact on cooling performance is less than the others, mainly because there is not much space available in the tangential direction to change during an optimization effort. A blowing rate range from 0.4 to 1.0 is considered without and with casing relative motion. This paper is an extension of a previous study by the first author [34], which is position optimization of film cooling holes on a squealer turbine blade tip.

## 2. Mathematical Models

### 2.1 Turbulence Model

Turbulent flow prediction is crucial for turbomachinery aerodynamics and heat transfer studies. There are many turbulence models for the numerical solution of high Reynolds number turbomachinery flows resolved by Reynolds Averaged Navier Stokes Equations (RANS). The most widely used two-equation models are k- $\epsilon$  and k- $\omega$  turbulence models for turbomachinery flows. Wilcox [35] published a comparative study of these models and stated that the k- $\omega$  model is consistent for all pressure gradients differently from the k- $\epsilon$  model. Menter [36] also presented an SST k- $\omega$  model for adverse pressure gradients. The present study used the incompressible SST k- $\omega$  model of turbulence [36].

### 2.2 Objective Functions & Non-Dimensional Variables

This section defines the objective functions of the optimization study and the non-dimensional flow and heat transfer parameters. The static pressure coefficient is defined as follows:

$$C_p = \frac{p - p_i}{0.5\rho U_i^2} \quad (1)$$

where  $p$  is mass-averaged local static pressure.  $p_i$  denotes the mass-averaged static pressure at the cascade inlet as the reference pressure of the non-dimensional  $C_p$ . The denominator of equation (1) is the cascade inlet dynamic head, where  $U_i$  is the cascade inlet velocity.

Aerodynamic performance is one of the main objectives of this study. The total pressure coefficient  $C_{p0}$  is described in equation (2), where  $U_m$  is the mean blade speed at midspan, taken from the Axial Flow Turbine Research Facility (AFTRF) of Pennsylvania State University [25,49,50,51]. The total pressure loss coefficient, defined in equation 3, is used to compare the aerodynamic performance of the cases.  $C_{p0}$  is calculated on the plane located at 0.25  $C_x$  downstream from the HP turbine airfoil's trailing edge. The specific HP turbine airfoil under investigation is identical to the rotor tip profile of the AFTRF test rig [49].

$$C_{p0} = \frac{p_0 - p_{0i}}{0.5\rho U_m^2} \quad (2)$$

$$\Delta C_{p0} = \frac{\iint \rho u C_{p0} dy dz}{\iint \rho u dy dz} \quad (3)$$

The heat transfer rate on the cavity surface, as defined in equation (7), is another objective of this optimization effort.  $q_w''$  is the rate of thermal energy transfer per unit area per unit time by forced convection. An open-source

code is used to calculate wall heat flux in OpenFOAM® [37]. It calculates wall heat flux using turbulent and effective heat conductivity, defined in equations (4) and (5).

$$\kappa_t = \nu_t / Pr_t \quad (4)$$

$$\kappa_{eff} = \nu / Pr + \kappa_t \quad (5)$$

$$q''_w = \kappa_{eff} C_p \rho \nabla T \quad (6)$$

$$q_w = \iint q''_w dx dy \quad (7)$$

$$h = \frac{q''_w}{T_w - T_{0i}} \quad (8)$$

Solving 3-dimensional complex flow models using CFD is time-consuming, and a large number of cases should be solved for a multi-objective optimization study. Therefore, an artificial neural network (ANN) effectively reduces the overall computational time. The ANN used is trained using a database that has been generated by using CFD predictions.

### 2.3 Artificial Neural Network & Optimization Algorithm

The database created to train the ANN is divided into training and testing. Here, the training data is used to develop the network and testing data is used to test the prediction accuracy of the network. In this study, 70% of the database has been used for testing, and 30% has been allocated for training. The mean square error, defined in equation (9), selects the best network. Here,  $\hat{Y}_i$  represents network predictions for testing data, and  $Y_i$  represents the actual testing data obtained using CFD. A Feed Forward Neural Network (FFNN) is used for function approximation. There are many successful optimization studies using FFNN as an approximation tool [38-43]. Maral et al. [42] have tested three different surrogate models for their optimization algorithm. These were Artificial Neural Network (ANN), Support Vector Machine (SVM) and Extreme Learning Machine (ELM). And they reported that ELM is the fastest; however, ANN gives the best predictions out of these three models. As a result of these findings, ANN is selected as the surrogate model to use with the optimization algorithm. The neural network package of the open-source software Octave [44] is used for constructing the ANN. A single hidden layer is used in the ANN, and the number of neurons in the hidden layer is selected so that the resulting ANN yields the minimum mean square error MSE. The procedure used in [41 - 43] is also followed here for this purpose.



$$MSE = \frac{1}{n} \sum_{i=1}^n (\hat{Y}_i - Y_i)^2 \quad (9)$$

Unlike single-objective versions, multi-objective optimization studies produce more than one optimum solution. The solutions not dominated by other solutions in both objectives are defined as Pareto optimal solutions. A non-dominated sorting genetic algorithm NSGA-II [40] is one of the most widely used algorithms for multi-objective optimization studies because of its ability to find convergent solutions to difficult problems [46-48]. It generally uses the Darwinian principle, which selects the fittest and non-dominated solutions, creating Pareto optimal solutions. It also uses crowding distance and the non-dominated rank to preserve diversity.

### 3. Methodology

#### 3.1 Geometric Details of the HP Turbine Blade

The HP turbine blade used in this investigation belongs to the Axial Flow Turbine Research Facility (AFTRF), operational at the Pennsylvania State University. **The research facility and airfoil design details are given in Camci [49,50,51].** The tip profile of the AFTRF rotor airfoil, as shown in Fig.1, is used to form an extruded solid model of the blade tip for the present calculations. Appendix-1 presents the airfoil coordinates of the tip section of the airfoil. The design specifications of the linear cascade used throughout the current computations are given in Table 1. A sketch depicting the linear cascade's main geometrical parameters is shown in Fig. 1, and the manufacturing coordinates of the tip airfoil section are given in Appendix 1. Senel et al. [33] also used the same tip geometry without the cooling holes as a part of their investigation to see the effect of squealer width and height on aerothermal performance.

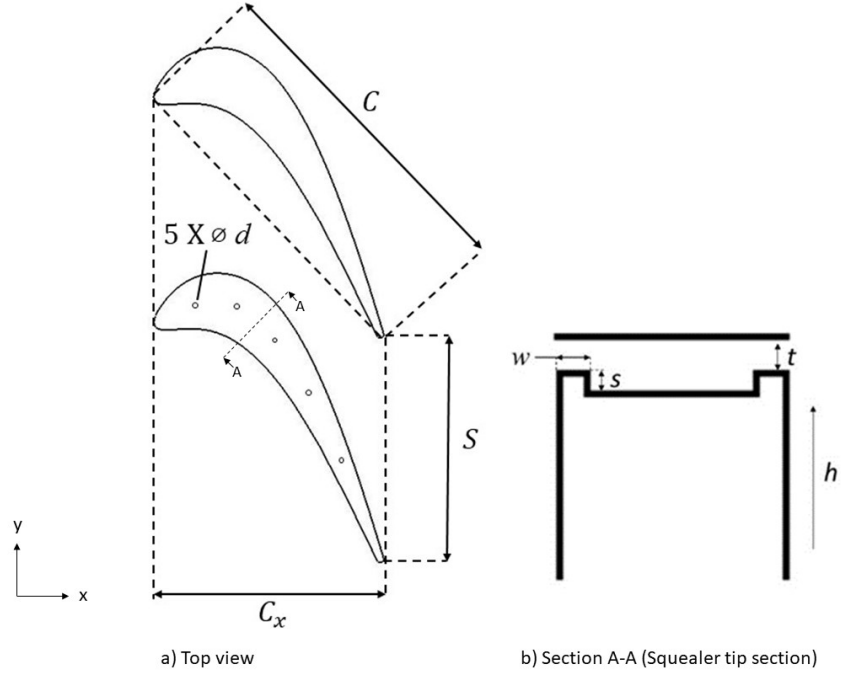


**Figure 1:** Geometric details of the AFTRF tip airfoil.

**Table 1:** Geometric characteristics of AFTRF turbine blade [33].

<i>Geometric Parameter</i>	<i>Value</i>
Blade Chord, $C$	121.5 mm
Blade Axial Chord, $C_x$	85.04 mm
Blade Span, $h$	123 mm
Blade Pitch, $S$	99.274 mm
Tip Clearance, $t$	1.23 mm
Squealer Width, $w$	2.101 mm
Squealer Height, $s$	1.2 mm
Inlet Flow Angle, $\alpha$	$71.3^\circ$
Film Cooling Hole Diameter, $d$	1.125 mm

The computational domain in this investigation is formed as a linear turbine cascade arrangement without and with casing motion. Special attention is paid to generating film cooling holes on the squealer tip cavity platform. A periodic boundary condition is imposed in the circumferential direction ( $y$ ). An ideal linear cascade arrangement corresponds to a flow system with an infinite number of blades where perfect circumferential periodicity exists. The same relative inlet flow conditions of the AFTRF rotor are imposed in the cascade.

The boundary conditions for the current linear cascade arrangement are shown in Table 2. While the coolant to free stream temperature ratio is taken as 0.5, the average wall to free stream temperature ratio is used as 0.7

to comply with the realistic operational conditions in a typical present-day aero-engine.

The cooling holes are positioned inside the squealer cavity floor using 14 mm spacings along the axial chord length. The positions of four film cooling holes in the  $y$ -direction of the blade are free to change as optimization variables. The fifth hole, which is too close to the trailing edge, is fixed on a specific position.

**Table 2:** Boundary conditions for the computations in the linear cascade with AFTRF tip profile.

<i>Geometric Parameter</i>	<i>Value</i>
Inlet Velocity	(27.2, 8.6, -2.2) m/s
Outlet Pressure	-3595 Pa
Inlet Temperature	440 °K
Wall Temperature	308 °K
Film Cooling Inlet Temperature	220 °K
Blowing Ratio ( $M=\rho_c U_c / \rho_\infty U_\infty$ )	1.0 and 0.4

### 3.2 Grid Generation

For a population-based optimization study, too many predictions may be required to optimize the objectives, and the number of analyses increases with an increasing number of input variables. Four input variables exist in the present study. These are the normalized film cooling hole positions between the suction and pressure sides. The subsequent computational runs usually increase the elapsed time of the optimization process and computational cost. Grid generation is typically required each time when positions of film cooling holes are changed. However, *topoSet* and *createPatch* utilities of the OpenFOAM® software provide a solution to change the cooling positions without requiring new grid generation at each step. This automatic grid updating feature significantly lightens the computational effort. A new grid is generated with densification on the lines where the positions of film cooling holes are optimized. The fifth line close to the trailing edge is not used during the

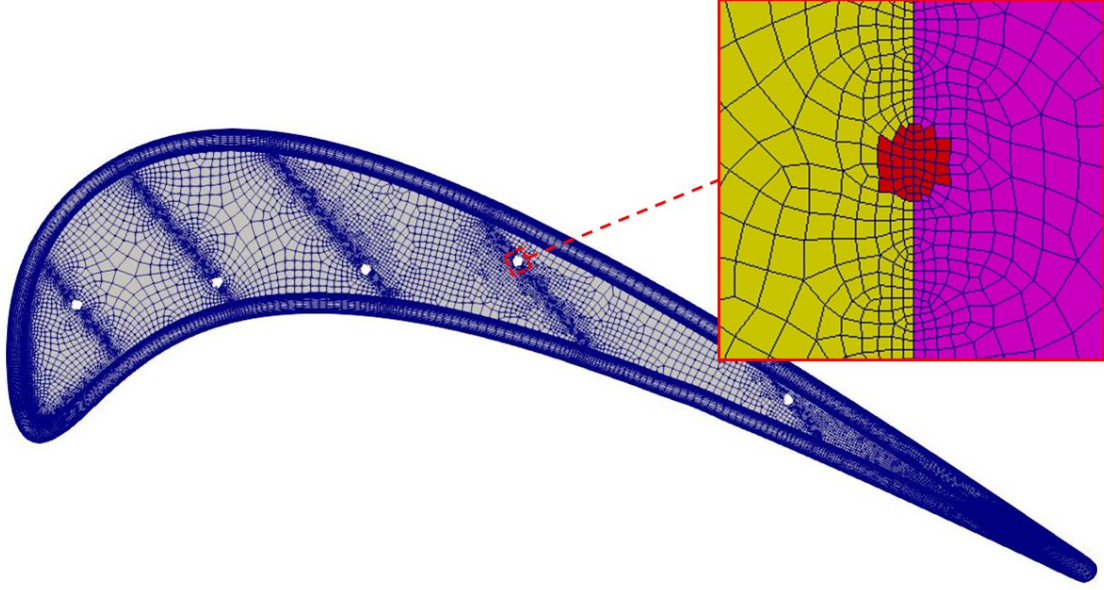


**Figure 2:** The automatic grid updating feature with densification on the lines where the positions of film cooling holes are optimized.

optimization. Its location is fixed on the mean camber line. The grid structure and a detailed view of the cooling hole region are given in Figure 2. A mesh dependency test was conducted using 4.5, 6.7, 7.2, 7.8 and 8.4 million cells. The static pressure coefficient distributions at the mid-span from each grid measure are shown in Figure 3. There is almost no difference between the results with different mesh densities.

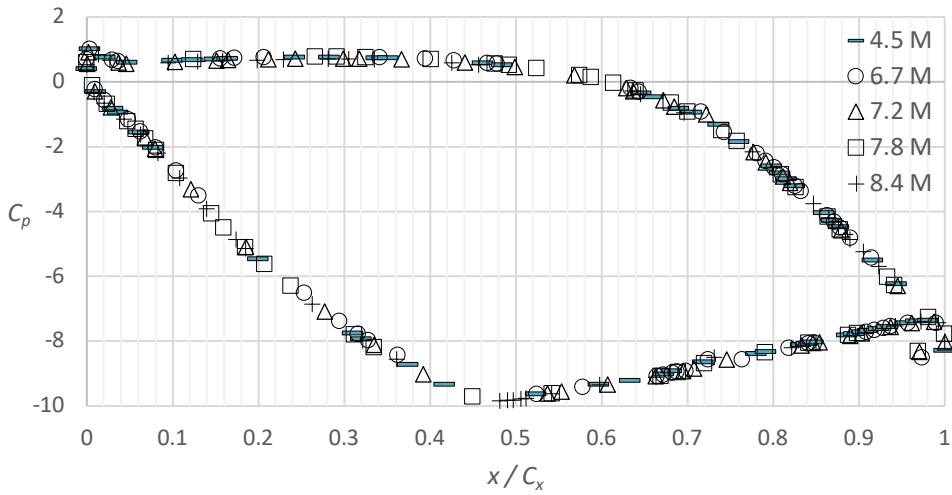


**Figure 3:** Mesh dependency study for the the linear cascade with AFTRF tip profile.

The heat transfer results are generally more sensitive to mesh resolution. The heat transfer coefficient distributions on the camber line of the squealer tip floor are shown in Figure 4. The tip platform area is obviously a

more challenging region regarding the dependency of the computed heat transfer rates on the mesh density. Figure 4 shows that the results from the 4.5 Million grid cells deviate visibly from all other grids in almost all locations along the camberline. However, starting from the 6.7 million cell grid, all four grid resolutions show similar  $h$  distributions along the camberline, except the highly three-dimensional leakage flow start-up region between 0.12 and 0.35 of the normalized arc length. This intermittent region is the location where the three dimensionality of the leakage flow starts to be more influential. The impingement and separation features of the local vortical structure are marked as relatively higher and lower heat transfer regions. The grid sensitivity in this narrow area is slightly higher. The  $h$  distribution outside this band is not measurably sensitive to the grid measure for 6.7, 7.2, 7.8 and 8.4 million grid cells.

The mesh with 7.8 million cells was selected to run the cases because of the densification necessity of the hole movement feature. Figures 3 and 4 indicate a good mesh independency level for the computational aero-heat transfer effort in this study. The average  $y^+$  value on the tip section is around 0.13 for the generated grid. A maximum  $y^+$  value of around 3.9 occurs only at a few points on the squealer rim near the trailing edge. The  $y^+$  distribution on the camber line of the squealer cavity platform is shown in Figure 5. The highly three-dimensional leakage flow start-up region between 0.12 and 0.35 is also apparent in the  $y^+$  distribution in Fig.5 as the reflection of the highly three-dimensional and recirculatory leakage flow. However, the  $y^+$  values on the camber line are all less than one.

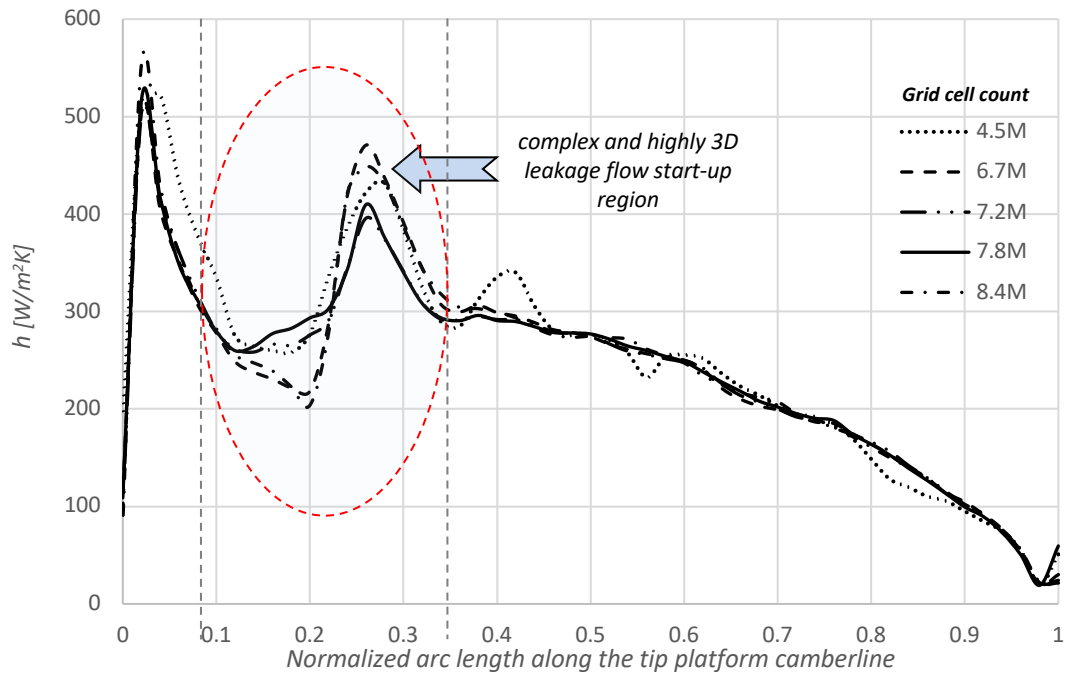


**Figure 4:** Mesh dependency,  $h$  versus *normalized arc length* on the camber line of squealer cavity floor.

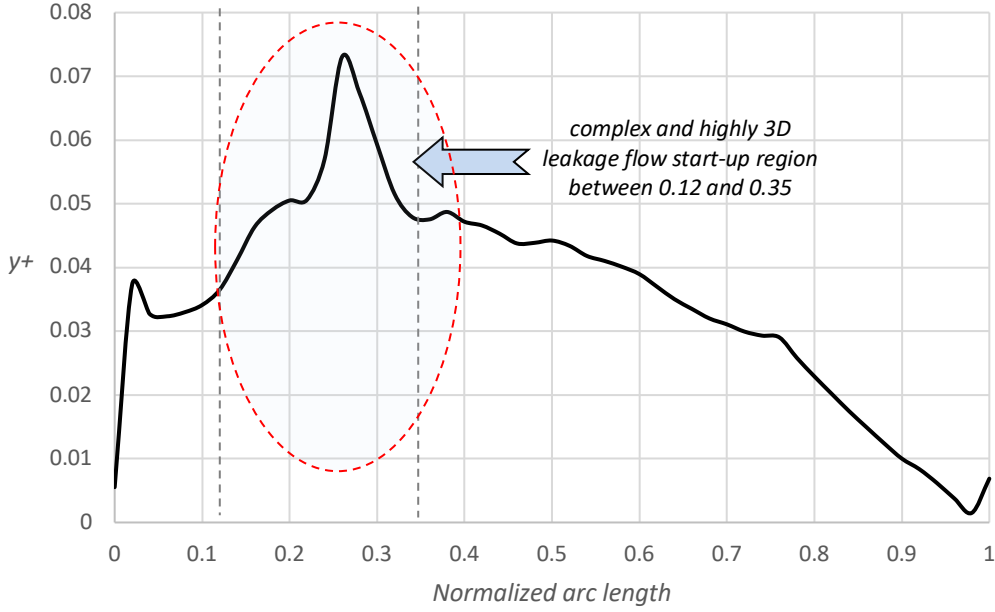


**Figure 5:**  $y^+$  versus *normalized arc length* on the camber line of squealer cavity floor.

### 3.3 Automated grid updates for new cooling hole locations

The same grid was used for all cases, with automated modifications required for different film cooling hole locations. Automatic grid modifications effectively reduced the total optimization time and complexity. The *topoSet* utility of OpenFOAM® was used with a cylindrical selection option, and cell faces were selected on the lines where a grid densification was imposed, as shown in Figure 2. Figure 6 shows a representation of a cylindrical selection of *topoSet* utility. The boundary type is changed from wall to inlet by using *createPatch* utility of OpenFOAM® repeated for all film cooling inlets.

However, this technique has minor disadvantages for coarse grids because the mesh structure does not become a perfect circle around the cooling hole, as shown in Figure 6, after subsequent updates. Thus, the mesh structure is kept denser on the lines on which the positions of film cooling holes are optimized. The RANS computation time per case increases because of artificially increased mesh density. However, an automated update is still better than generating a brand-new mesh for all cases. The effect of the very slight geometric difference of holes in the updated mesh structure is neglected in this study. The relative standard deviations of mass flow rates are 4.7%, 4.3%, 3.1% and 5.4% from the 1<sup>st</sup> to 4<sup>th</sup> film cooling hole.

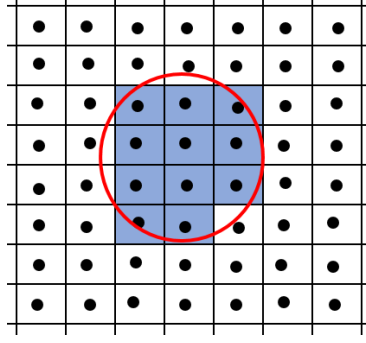


**Figure 6:** Representation of cylindrical selection.

### 3.4 Boundary & Initial Conditions

Figure 7 shows the computational domain of the cascade model with its boundary conditions. The domain is divided into three parts; inlet, rotor, and outlet. The domain's sides are imposed as periodic boundary conditions by the cascade flow assumptions, and other boundaries are defined as no-slip walls except for the inlet and outlet.

Velocity inlet and pressure outlet conditions are used at the inlet and exit of the domain. Values of boundary conditions are given in Table 2, and the turbulence intensity of the inlet at mid-span is set to 0.5% as measured in the AFTRF operation [49], [50], [51].

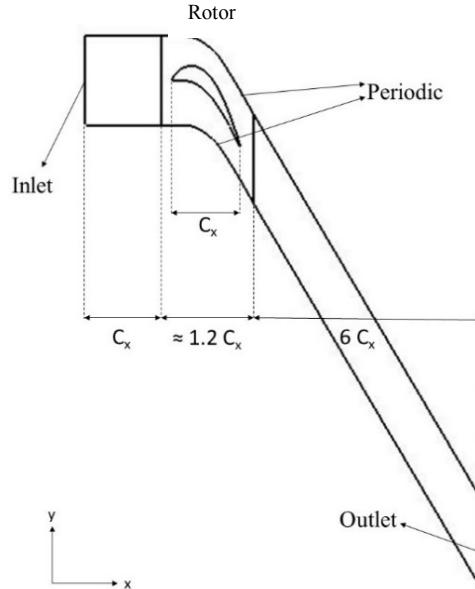


**Figure 7:** Boundary conditions on the computational domain forming the linear cascade of the AFTRF tip profile.

The blowing ratio is a critical variable that changes cooling performance because the coolant flow should have enough energy to surpass the tip flow and create a proper coolant layer on the tip surface. Many studies showed that increasing the blowing ratio increases the cooling performance [18], [19], [20]. However, over an optimal injection rate, the film coolant penetrates the free stream and starts to lose its cooling effectiveness near the wall. A high blowing ratio also reduces the turbine efficiency by consuming too much air from the cycle. The blowing rate was initially selected equal to 1.0 throughout this optimization approach.

Additionally, a low blowing ratio (0.4) case and casing relative motion case were also studied to see their effects on aerodynamic performance and heat transfer on the tip region. The speed of the casing relative motion is taken from the AFTRF experiment [51], which is 663.5 m/s, as calculated from the rotational speed of 1322 rpm.

### 3.5 Validation of the Aero-heat Transfer Effort

**Aerodynamic Validation:** The CFD effort was validated using a turbine blade profile experimentally studied by Beer [52]. The predicted uncertainty  $\delta C_p/C_p$  of the measured pressure coefficient is 0.6 % with a 95 % confidence level. The  $C_p$  distribution measured at the mid-span of the airfoil in a linear cascade arrangement was compared to the current computational aerodynamics data in Figure 8. The computed  $C_p$  over the airfoil surfaces follows the experimental measurement points well. There is a slight discrepancy over  $x/C_x=0.7$  on the aft part of the airfoil surface. This region corresponds to a diffusion zone with a mild adverse pressure gradient on the suction side. However, this slight discrepancy is within the measurement error.

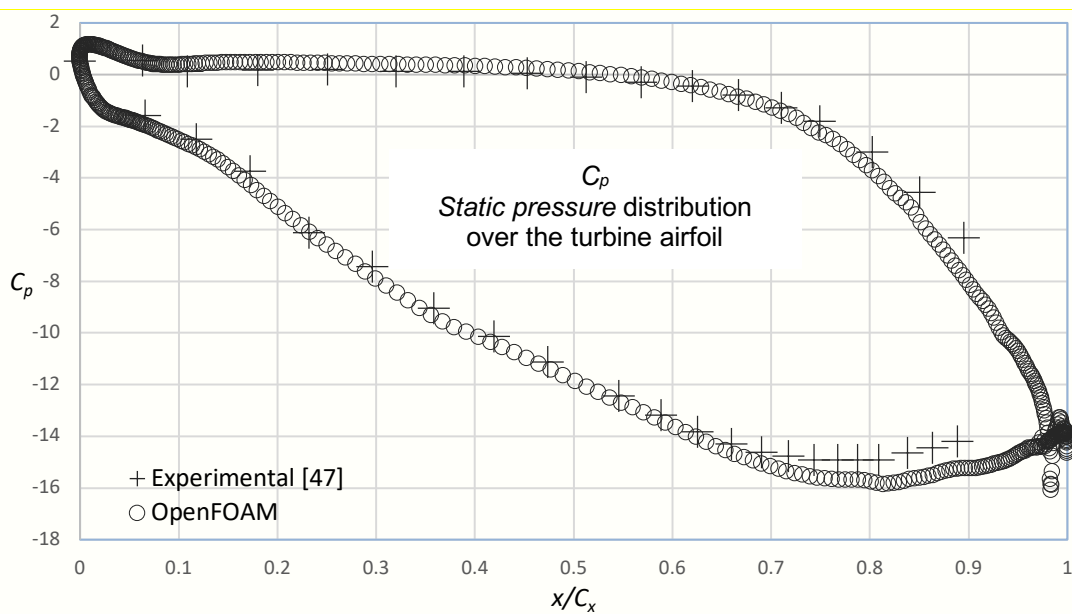


**Figure 8:** Comparison between the experimental blade loading data of Beer [52]  $C_p$  and the current computational results.



**Computational Heat Transfer Validation:** Validation of the computed heat transfer is also crucial for this study. An experimental heat transfer data set on the suction side of the SM701 airfoil obtained by Klaput [53] in the low-speed wind tunnel of the Pennsylvania State University is used to validate the current heat transfer computations. This airfoil was selected because of the availability of high-resolution convective heat transfer data on its suction side. The uncertainty of the measured heat transfer coefficient  $h$  is  $\delta h/h=6\%$ . A heat transfer measurement method based on thermographic liquid crystals was employed by Klaput [53]. The airfoil coordinates of SM701, having a chord length of 304.8 mm, are listed in Appendix-2. This airfoil was originally designed by Maughmer and Somers [54],[55]. The measured heat transfer coefficient on the suction side of the SM701 airfoil is compared to the current CFD result in Figure 9. The suction side of the airfoil simultaneously contains distinct laminar, transitional and fully turbulent zones making the prediction of convective heat transfer rates a challenging task. The current heat transfer computations used the Langtry-Menter two-equation shear stress transport SST model [56] for turbulence modeling. A momentum thickness Reynolds number  $Re_\theta$  based intermittency  $\gamma$  model in the transitional flow regime is used. There are a total of four turbulence handling equations used in the transitional flow regime. The computational and experimental results show good agreement, and CFD results also predict the transition and turbulence region well till  $x/C_x=0.80$ , as shown in Figure 9. The transitional flow zone is between  $x/C_x=0.68$  and  $0.78$ . Between  $x/C_x=0.80$  and  $1$ , the fully turbulent

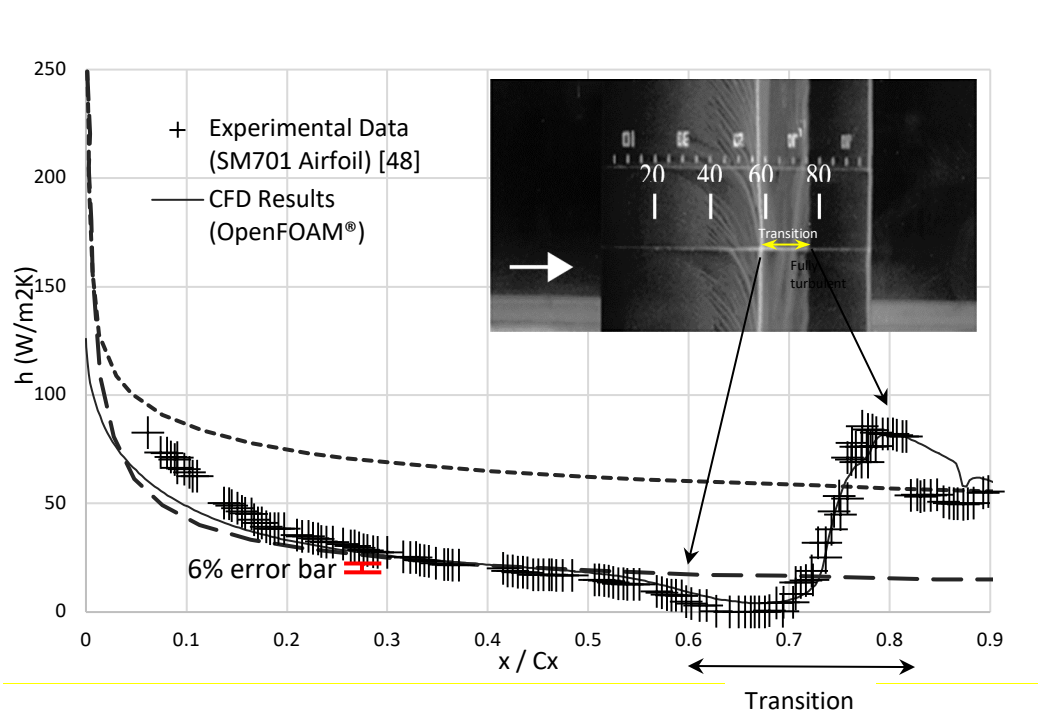


**Figure 9:** Comparison between experimental heat transfer data of Klaput [53] and the present heat transfer computations on the suction surface of SM701 airfoil.

region starts with the addition of some trailing edge separation, as indicated in the surface flow visualization image of Figure 9. The CFD model properly catches the general trends of  $h$  on most of the airfoil surface when compared to measured  $h$  with an uncertainty of  $\delta h/h=6\%$ . The region after  $x/C_x=0.80$  is also a relatively high uncertainty zone for the heat transfer experiments because the copper electrodes of the Inconel constant heat flux surface tend to slightly disturb the otherwise smooth heat transfer surface.

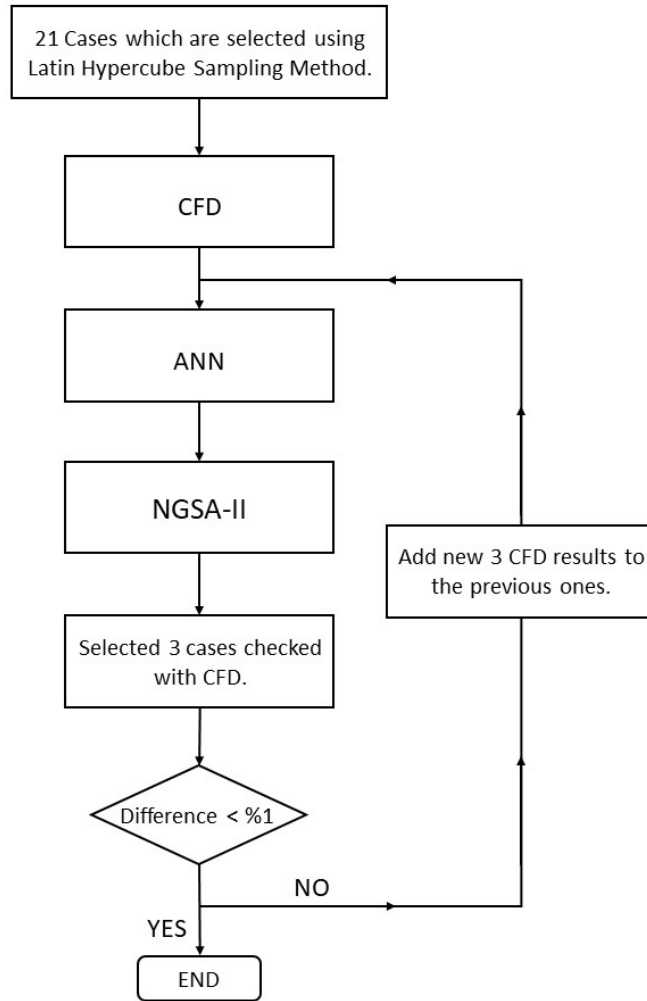
### 3.6 Optimization Process

Objective function predictions for the NSGA-2 algorithm are performed using ANN, which was trained using a database created from the present CFD predictions. A suitable size of the database is not known a priori. Therefore an initial database consisting of 21 elements is created for this process, and Latin hypercube sampling [57] is used to specify the values of inputs for these cases. After the first optimization process, three design points are selected from the Pareto curve. Two of these points are from the ends of the Pareto front, which yield minimum heat transfer and minimum aerodynamic loss, the third one is from the mid-part of the front, which assumes both objectives have equal importance. Additional CFD results are obtained for these points and are compared with their corresponding ANN predictions. These three new design points and their CFD solutions are added to the database, and training of the ANN and the optimization process is repeated. This loop continues until the relative difference between the CFD and ANN predictions falls below 1% for all three selected designs. The flow chart of the optimization process is shown in Figure 10. The positions of the four film cooling holes in the  $y$ -direction are normalized between 0 and 1, as shown in Figure 11. Table 4 shows the normalized values used as input parameters. The fifth hole is not used as a design variable, and its position is fixed to decrease the number of computational runs and the optimization cost. Also, the fifth hole is in a narrow region near the trailing edge wedge zone. Thus, manufacturing limitations may not allow flexibility to change its position easily. Two ANNs are constructed for the two objective functions. The ANNs constructed contain four input neurons, one output neuron, and a hidden layer consisting of hidden neurons whose number changes between 1 and 10. The networks were trained ten times for each hidden layer configuration, and the ANN with the minimum overall error was selected. NSGA-II algorithm, which was also used in the previous articles by the authors [41,43], is used for the optimization process with the best network. The population contains 100 individuals, and the process is run for 200 generations. All other parameters are specified in Table 3.

The current optimizations' objective functions are the total pressure loss coefficient and the integrated wall heat flux on the cavity surface. Figure 12 presents the last five Pareto fronts obtained using NSGA-II + ANN

**Table 3:** NSGA-II Parameters

<i>Parameter</i>	<i>Value</i>
Population Size	100
Generation Number	200
Mutation Rate	0.2
Crossover Rate	0.8
Mutation Index	20
Crossover Index	20
Tournament Size	5

**Figure 10:** Flow chart of the optimization process.

and all of the CFD results. The Pareto fronts show convergence for cavity heat flux rate ( $q_{\text{cavity}}$ ) values less than  $73 \text{ W/m}^2$ . The agreement between the CFD and ANN predictions close to the Pareto front is better than the other locations. There are a few CFD predictions that dominate the Pareto front. However, one can note the

rather short range of the aerodynamic loss coefficient. For this reason only heat transfer rate predictions were used to calculate the relative error between ANN and CFD predictions.

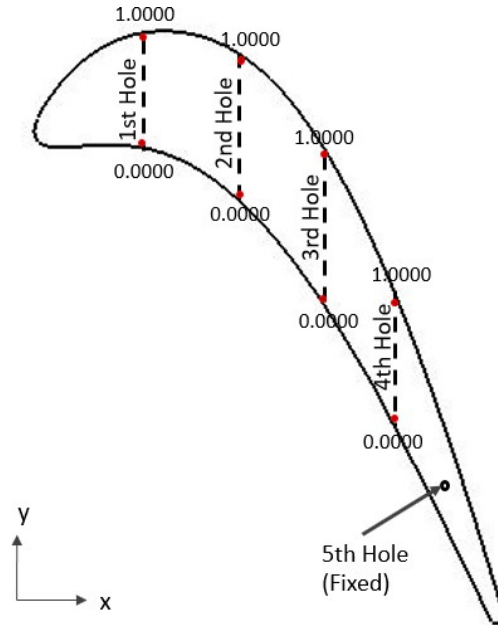


**Figure 11:** Normalization of hole positions between 0 and 1.

**Table 4:** Design points of film cooling holes.

<b>Case #</b>	<b>Design Points</b> (Normalized Between 0 and 1)				<b>Case #</b>	<b>Design Points</b> (Normalized Between 0 and 1)			
	<b>1<sup>st</sup> Hole</b>	<b>2<sup>nd</sup> Hole</b>	<b>3<sup>rd</sup> Hole</b>	<b>4<sup>th</sup> Hole</b>		<b>1<sup>st</sup> Hole</b>	<b>2<sup>nd</sup> Hole</b>	<b>3<sup>rd</sup> Hole</b>	<b>4<sup>th</sup> Hole</b>
1	0.4992	0.6890	0.0344	0.7471	27	0.0488	0.5713	0.1790	0.2920
2	0.7146	0.9571	0.0432	0.2347	28	0.0840	0.0000	0.4411	0.4217
3	0.8641	0.0219	0.7375	0.9913	29	1.0000	1.0000	0.0000	0.0000
4	0.6685	0.6461	0.4258	0.8051	30	0.3456	0.2985	0.0000	0.9076
5	0.3486	0.3075	0.3515	0.3113	31	0.0008	1.0000	0.7105	0.9975
6	0.4094	0.8708	0.6969	0.6186	32	0.0979	0.9113	0.0000	0.9357
7	0.6221	0.2373	0.2986	0.4326	33	0.4349	0.1567	0.1651	1.0000
8	0.1200	0.4381	0.4702	0.8265	34	1.0000	1.0000	1.0000	1.0000
9	0.0842	0.4218	0.6093	0.2856	35	0.4633	0.0463	0.0838	0.4102
10	0.2192	0.8344	0.7624	0.0938	36	0.3921	0.7527	0.2568	0.5747
11	0.4426	0.7973	0.2558	0.5615	37	0.3505	0.0000	0.2592	0.7526
12	0.9734	0.2681	0.5689	0.8831	38	0.6481	0.0000	0.6182	0.2880
13	0.5830	0.3494	0.8245	0.1844	39	0.3401	0.0000	0.7686	0.0000
14	0.2859	0.0872	0.1007	0.3805	40	0.2081	0.6324	0.4485	0.4500
15	0.2399	0.7486	0.5072	0.6320	41	0.1948	0.5323	0.3962	0.4285
16	0.8317	0.6096	0.3898	0.0308	42	0.5039	0.0000	0.2058	0.6021
17	0.9065	0.1812	0.2357	0.9152	43	0.4972	0.3085	0.2917	0.5805
18	0.5659	0.1273	0.1788	0.6935	44	0.5289	0.1947	0.2816	0.6182

19	0.1880	0.4819	0.6308	0.5030	45	0.5242	0.2361	0.3889	0.6313
20	0.0331	0.9299	0.8577	0.1405	46	0.5498	0.3490	0.3819	0.6527
21	0.7819	0.5522	0.1451	0.4262	47	0.5447	0.3482	0.3800	0.7153
22	0.8491	0.0788	0.0000	0.0000	48	0.6013	0.3968	0.0190	0.8543
23	0.2069	1.0000	1.0000	0.0000	49	0.5633	0.3661	0.0173	0.8638
24	0.0000	0.9995	0.8732	0.0009	50	0.5145	0.4236	0.0163	0.8621
25	0.0000	1.0000	1.0000	0.7576	<i>5th Hole is fixed on 0.3475</i>				
26	0.0601	0.0000	0.0000	0.0000					

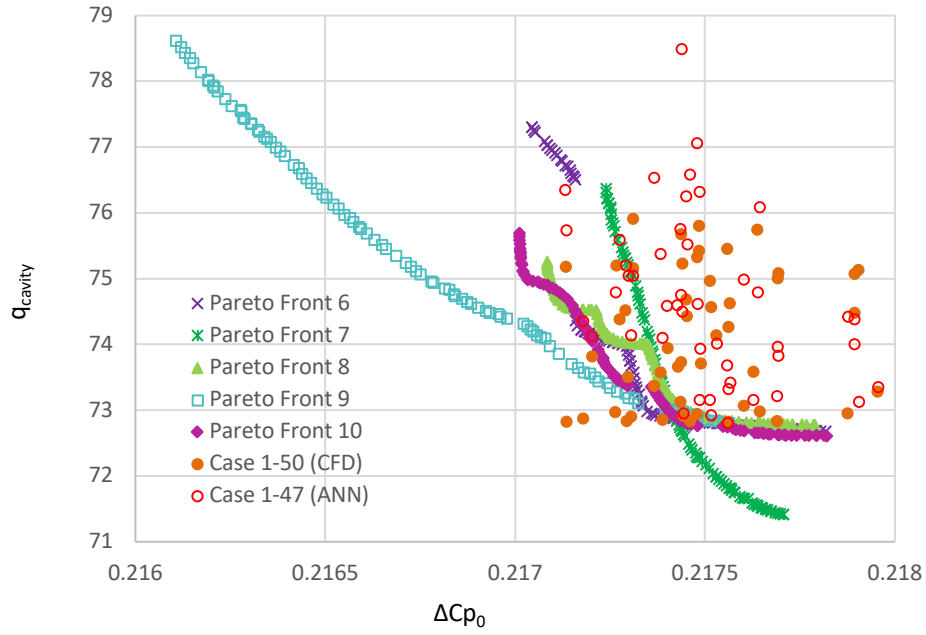


Figure 12: Pareto optimal solutions and results.

## 4. Results and Discussion

### 4.1 50 cooling configurations with a stationary casing at $M=1.0$

The CFD results of all 50 cases with different positions of film cooling holes and the result without film cooling holes (reference Case 0) are listed in Table 5. Initially, the relative motion of the casing is not taken into account.  $\Omega$  and  $\Gamma$  show the percent change in total pressure loss coefficient and total heat flux to the tip surface between the related case and the non-cooled reference case (Case 0).  $q_{total}$ ,  $q_{cavity}$ ,  $q_{tip}$  and  $q_{side}$  show, respectively, the total heat flux, heat flux on the cavity bottom surface, on the top surface of the rim and on the inner sidewall of the rim.

**The case with the minimum aerodynamic loss and best cooling performance:** A reduction in heat transfer to the tip with film cooling is apparent for most cases. A 13.43 % reduction in  $q_{total}$  is observed for Case

44, Table 5. On the other hand, the changes in the aerodynamic loss coefficient  $\Omega$  are quite similar and small for all 50 film-cooled cases. There is obviously an aerodynamic loss for all 50 cases, but the magnitude of it is relatively small compared to the sum of the boundary layer, wake, secondary flow and tip vortex losses in the passage. The aerodynamic loss change  $\Omega$  of the cooled case in reference to the uncooled tip increases from a minimum of 0.23% to the maximum value of 0.61%, 0.39% being the average of all fifty cases. It is observed that the aerodynamic loss increase computed at the exit plane is not significantly large because of the relatively small amount of air mass flow rate injected from the five discrete holes for all cases for a blowing rate of  $M=1.0$ . Case 50, as the optimum solution of the multi-objective study, comes with a 0.31% aerodynamic loss increase and a 12.95% reduction in total heat flux, as shown in Table 5. Since the case-to-case variation of the aerodynamic loss is quite small, one can also choose to work with the maximum heat flux reduction case, Case 44.

**Influence of coolant injection on flow and heat transfer field near the tip section (optimal case):** The velocity magnitude contours on the five sections where film cooling holes are located are shown in Figure 13 for  $M=1.0$  for stationary casing. No-film cooling case and Case 50, which is the optimal 'heat transfer and aerodynamic loss' solution are compared. The local flow separation called the vena-contracta effect just downstream of the pressure side corner of the tip leakage zone is shown in Figure 13.a. Most of the leakage fluid travels to the suction side near the casing, as shown by the yellow-red contours. The top of the pressure side rim is a high heat transfer zone, as shown by the red contours in Fig. 13.a. The second, third and fifth coolant jets cool the cavity platform effectively near the pressure side rim. The protective cooling fluid shown with green and blue areas usually tends toward the pressure side rim near the cavity floor except for the first hole. The first hole's effective cooling action is near the suction side rim, as indicated by a green zone. The fourth hole from the leading edge protects a zone near the suction side rim, as shown in the green area. The fifth hole occupying the trailing edge wedge area is highly effective in protecting the cavity bottom and rim surfaces, as shown with a dark blue color.

**Influence of coolant injection on total pressure loss at the exit plane (optimal case):** The effect of tip leakage flow on the total pressure coefficient at the exit plane located at  $x=1.25C_x$  is presented in Figure 14. The flow areas with negligible aerodynamic losses are represented with yellow zones. The highest aerodynamic losses are in the tip leakage vortical structure near the suction side corner of the main flow, as marked by dark blue color. The second important high-loss area is in the wake of the airfoil extending from the hub to tip, as indicated by the color band between orange and light red. The secondary flow-related loss at the exit plane is marked by a small

**Table 5:** Results of optimization objectives (aerodynamic loss and heat transfer)  
for a blowing rate of M=1.0, with STATIONARY casing  
( $\Omega$  and  $\Gamma$  values show the relative difference with respect to Case 0, no-film cooling).

$$\Omega = \frac{\Delta C_{p0,FC} - \Delta C_{p0,NoFC}}{\Delta C_{p0,NoFC}} \quad \Gamma = \frac{q_{total,FC} - q_{total,NoFC}}{q_{total,NoFC}}$$

Case # (i)	$\Delta C_{p0}$	$\Omega$	$q_{cavity}$ [W]	$q_{up}$ [W]	$q_{side}$ [W]	$q_{total}$ [W]	$\Gamma$
0 (NO FC)	-0.21663	<b>0.00%</b>	-38.78	-31.93	-13.40	-84.11	<b>0.00%</b>
1	-0.21731	<b>0.31%</b>	-33.77	-29.59	-11.69	-75.05	<b>-10.77%</b>
2	-0.21713	<b>0.23%</b>	-34.76	-29.53	-11.44	-75.74	<b>-9.95%</b>
3	-0.21764	<b>0.47%</b>	-35.28	-29.51	-11.30	-76.09	<b>-9.53%</b>
4	-0.21726	<b>0.29%</b>	-33.45	-29.62	-11.73	-74.80	<b>-11.07%</b>
5	-0.21763	<b>0.46%</b>	-31.44	-29.86	-11.86	-73.16	<b>-13.02%</b>
6	-0.21738	<b>0.35%</b>	-33.93	-29.60	-11.84	-75.38	<b>-10.38%</b>
7	-0.21756	<b>0.43%</b>	-31.90	-29.75	-11.66	-73.31	<b>-12.83%</b>
8	-0.21753	<b>0.41%</b>	-32.55	-29.78	-11.70	-74.02	<b>-11.99%</b>
9	-0.21730	<b>0.31%</b>	-32.69	-29.78	-11.67	-74.14	<b>-11.85%</b>
10	-0.21727	<b>0.30%</b>	-34.56	-29.52	-11.52	-75.60	<b>-10.12%</b>
11	-0.21744	<b>0.37%</b>	-33.20	-29.70	-11.85	-74.75	<b>-11.12%</b>
12	-0.21743	<b>0.37%</b>	-34.25	-29.74	-11.76	-75.76	<b>-9.93%</b>
13	-0.21720	<b>0.26%</b>	-32.82	-29.64	-11.66	-74.12	<b>-11.87%</b>
14	-0.21769	<b>0.49%</b>	-31.97	-29.73	-11.51	-73.21	<b>-12.95%</b>
15	-0.21718	<b>0.25%</b>	-33.02	-29.63	-11.69	-74.34	<b>-11.61%</b>
16	-0.21745	<b>0.38%</b>	-34.45	-29.50	-11.58	-75.52	<b>-10.21%</b>
17	-0.21760	<b>0.45%</b>	-33.98	-29.56	-11.45	-74.99	<b>-10.84%</b>
18	-0.21752	<b>0.41%</b>	-31.84	-29.61	-11.46	-72.91	<b>-13.31%</b>
19	-0.21743	<b>0.37%</b>	-33.04	-29.79	-11.77	-74.59	<b>-11.31%</b>
20	-0.21713	<b>0.23%</b>	-35.44	-29.49	-11.42	-76.35	<b>-9.22%</b>
21	-0.21729	<b>0.30%</b>	-33.84	-29.64	-11.56	-75.04	<b>-10.78%</b>
22	-0.21764	<b>0.46%</b>	-34.53	-29.20	-11.06	-74.79	<b>-11.07%</b>
23	-0.21748	<b>0.39%</b>	-35.62	-29.46	-11.25	-76.33	<b>-9.25%</b>
24	-0.21745	<b>0.38%</b>	-35.57	-29.36	-11.32	-76.25	<b>-9.34%</b>
25	-0.21737	<b>0.34%</b>	-35.51	-29.64	-11.38	-76.53	<b>-9.01%</b>
26	-0.21789	<b>0.58%</b>	-34.25	-29.20	-10.92	-74.38	<b>-11.57%</b>
27	-0.21748	<b>0.39%</b>	-33.45	-29.66	-11.51	-74.61	<b>-11.29%</b>
28	-0.21788	<b>0.57%</b>	-33.25	-29.72	-11.45	-74.42	<b>-11.52%</b>
29	-0.21748	<b>0.39%</b>	-36.36	-29.35	-11.34	-77.06	<b>-8.38%</b>
30	-0.21748	<b>0.39%</b>	-32.37	-29.42	-11.37	-73.15	<b>-13.02%</b>
31	-0.21746	<b>0.38%</b>	-35.53	-29.66	-11.40	-76.59	<b>-8.94%</b>
32	-0.21729	<b>0.31%</b>	-34.98	-29.21	-11.01	-75.20	<b>-10.59%</b>
33	-0.21749	<b>0.40%</b>	-32.87	-29.66	-11.40	-73.93	<b>-12.10%</b>
34	-0.21744	<b>0.37%</b>	-37.29	-29.73	-11.46	-78.48	<b>-6.68%</b>
35	-0.21769	<b>0.49%</b>	-32.70	-29.64	-11.49	-73.83	<b>-12.22%</b>
36	-0.21744	<b>0.37%</b>	-33.06	-29.64	-11.81	-74.50	<b>-11.42%</b>
37	-0.21795	<b>0.61%</b>	-32.14	-29.69	-11.52	-73.35	<b>-12.79%</b>
38	-0.21769	<b>0.49%</b>	-33.07	-29.54	-11.36	-73.96	<b>-12.06%</b>
39	-0.21789	<b>0.58%</b>	-33.23	-29.42	-11.36	-74.01	<b>-12.01%</b>
40	-0.21740	<b>0.36%</b>	-33.09	-29.76	-11.74	-74.58	<b>-11.32%</b>
41	-0.21739	<b>0.35%</b>	-32.60	-29.78	-11.72	-74.10	<b>-11.90%</b>
42	-0.21756	<b>0.43%</b>	-32.51	-29.68	-11.49	-73.69	<b>-12.39%</b>
43	-0.21790	<b>0.59%</b>	-31.54	-29.79	-11.79	-73.12	<b>-13.06%</b>
44	-0.21756	<b>0.43%</b>	-31.45	-29.71	-11.65	-72.81	<b>-13.43%</b>
45	-0.21751	<b>0.41%</b>	-31.55	-29.80	-11.80	-73.15	<b>-13.02%</b>

46	-0.21757	<b>0.43%</b>	-31.70	-29.87	-11.86	-73.43	<b>-12.70%</b>
47	-0.21744	<b>0.38%</b>	-31.42	-29.74	-11.77	-72.94	<b>-13.28%</b>
48	-0.21727	<b>0.29%</b>	-32.12	-29.49	-11.33	-72.95	<b>-13.27%</b>
49	-0.21731	<b>0.31%</b>	-32.42	-29.53	-11.37	-73.32	<b>-12.83%</b>
50	-0.21730	<b>0.31%</b>	-32.21	-29.56	-11.45	-73.22	<b>-12.95%</b>

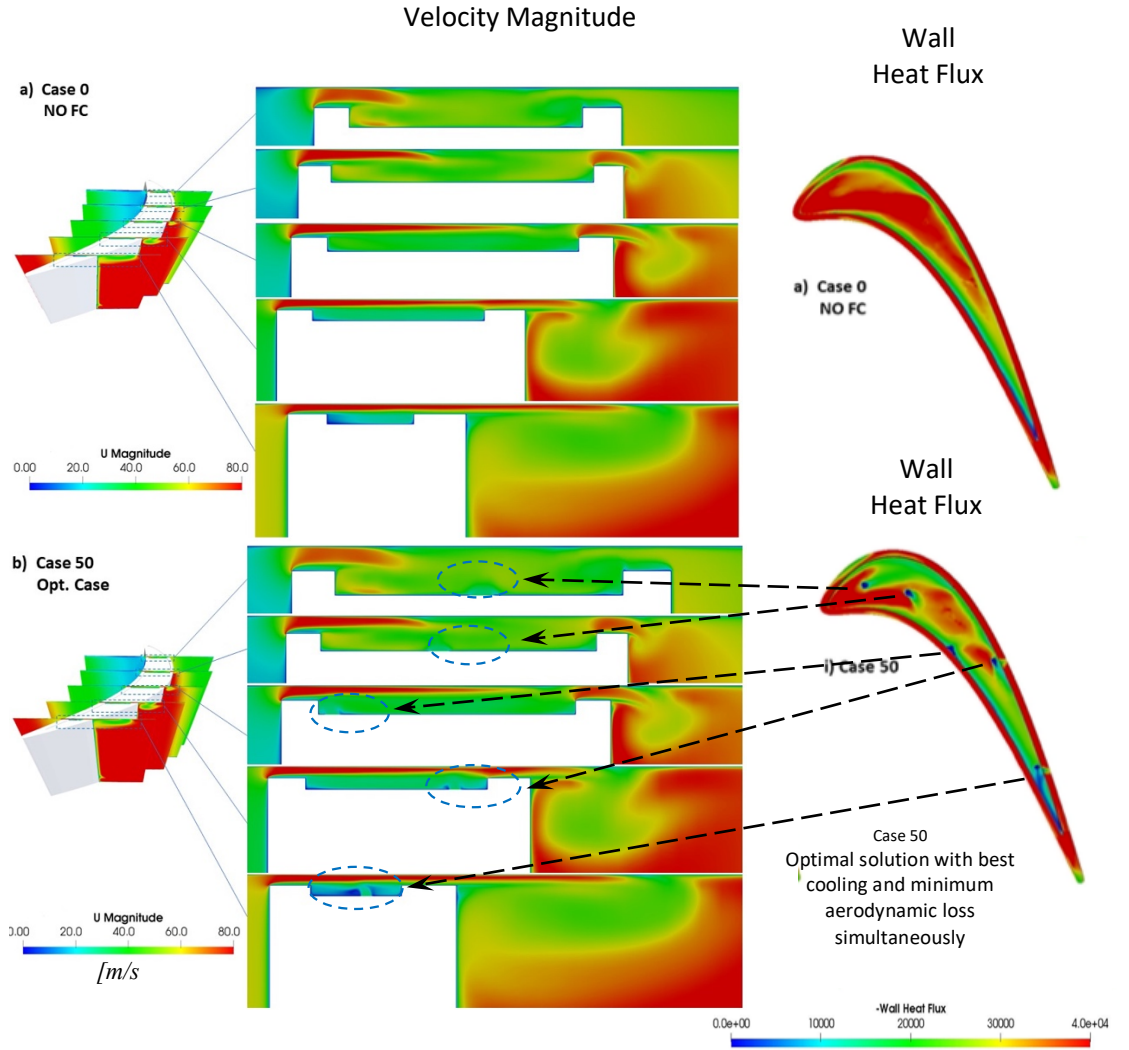


**Figure 13:** Velocity magnitude  $[m/s]$  and wall heat flux  $[W/m^2]$  contours, with STATIONARY casing (a) No film cooling case b) Case 50 (Optimal Case),  $M=1.0$ .

yellow area near the hub. The secondary flow vortex near the casing strongly interacts with the tip leakage vortex since they are counteracting. The tip vortex in the exit plane rotates in the clockwise direction, whereas the passage vortex spins in the counter-clockwise direction. The tip vortex usually dissipates most of the rotational energy of the tip passage vortex. An extremely thin endwall boundary layer also appears near the hub and casing surfaces, as colored by green. The aerodynamic loss level of the endwall boundary layers is slightly less than that of the



passage vortex. The influence of film cooling injection from the five discrete holes in each passage is not strongly felt in the total pressure field at the exit. This is mainly because of the small amount of the coolant mass flow rate compared to that of the mainstream and mixing occurring all the way down to  $x/C_x=1.25$ . However, non-negligible flow and heat transfer modifications locally exist just downstream of the discrete cooling holes, as shown in Figure 13.

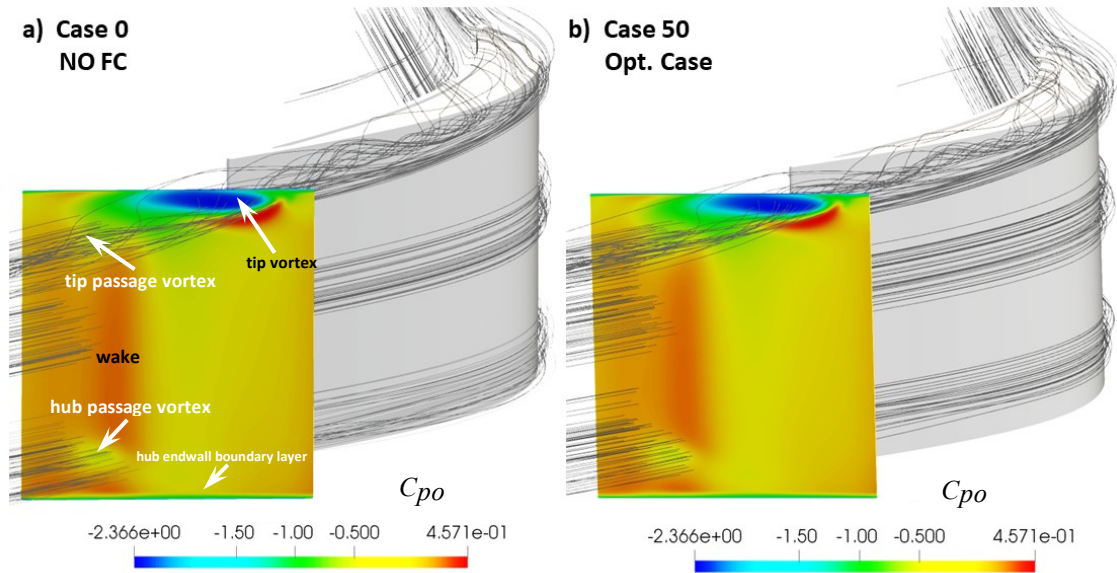


**Figure 14:** Total pressure coefficient  $C_{po}$  at exit plane ( $x=1.25C_x$ ), with STATIONARY casing,  $M=1.0$   
a) No film cooling case b) Case 50 (Optimum Case).

**Film cooling trajectories and local cooling performance for the optimal case:** The local cooling trajectories from the five discrete coolant jets for Case50 are presented in Figure 15 for a stationary casing. Case 50, as the optimum solution of the multi-objective study, comes with a 0.31% aerodynamic loss increase and a 12.95% reduction in total heat flux, as shown in Table 5. Most of the leakage fluid from the mainstream gases travels to the suction side near the casing, as shown in Figs.13 and 15. However, the coolant delivered by each hole joins the highly recirculatory flow pattern of the hot tip leakage fluid, as presented in Fig.15. The individual vortical flow structures over the cavity platform from the discrete coolant holes also act as aerodynamic loss generators. Although the cooling holes' main objective is to cool the cavity region, all five jets individually create their own 'normal jets incross-flow' situation resulting in high local strain rates. The coolant fluid stays within the boundaries of the conventional tip leakage vortex of the non-cooled case near the suction side of the airfoil once it exits from the top of the suction side rim into the mainstream, Fig.15.a.

The first, second and fifth holes are almost on the camberline for Case 50. The third and fourth holes are near the pressure side rim and suction side rim, respectively. Fig.13.a suggests that the top surface of the pressure

side rim is a high heat transfer zone, as shown by the red contours. Fig. 15.b shows that the second, third and fifth coolant jets cool the cavity platform effectively near the pressure side rim. The protective cooling fluid layer over the green and blue areas usually tends toward the pressure side rim near the cavity bottom, except for the first hole. The first hole's highly effective cooling action is near the suction side rim, as indicated by a green zone. The fourth hole from the leading edge protects a zone near the suction side rim, as shown with a green area. The fifth hole occupying the trailing edge wedge area is highly effective in protecting the cavity bottom and rim surfaces, as shown with a dark blue color. The top surfaces of the cavity rims are typically high heat transfer areas, as shown in Figure 15. However, the discrete coolant jets cool the areas locally when they pass over the suction side rim, especially for the third and fourth coolant jets, as marked by the dashed circular areas in Fig. 15.b. When the holes are placed near the pressure side or the camberline, there is no local cooling for the top surface of the pressure side rim.

#### ***4.2 Eight selected film cooling arrangements from the optimization study***

Eight specific cooling arrangements were selected from Table 5 out of 50 film cooling configurations for  $M=1$ , with stationary casing. The local wall heat flux values at the tip surface for the optimal solution are shown in Figure 16.(i), which is for Case 50. This case represents the best cooling and minimum aerodynamic loss case ( $\Gamma = -12.95\%$ ,  $\Omega = 0.31\%$ ). A search for the best cooling performance without imposing the minimum aerodynamic loss results in Case 44 as presented in Fig. 16.(h) with  $\Gamma = -13.4\%$  and  $\Omega = 0.43\%$ . Case 50 and 44 exhibit similar cooling and aerodynamic loss characteristics. Case 44 shows a small increase in  $\Omega$  to 0.43% from 0.31% of Case 50. Case 43 in Fig 16.(g) also indicates great cooling potential with a slightly elevated aerodynamic loss level, ( $\Omega = 0.59\%$ ,  $\Gamma = -13.06\%$ ). The cooling hole arrangement of Case 50 has the best aerodynamic loss character out of the last three cases discussed as 50, 44 and 43. The specific location of the third hole and the fourth hole in this case, plays an important role in weakening the tip leakage flow measurably. The information in Figure 16 suggests that discrete cooling holes located near the camberline have all viable cooling performances.

**The worst cooling case:** Case 34 has the worst cooling performance of  $\Gamma = -6.68\%$  at an acceptable aerodynamic loss level of  $\Omega = 0.37\%$ . One should note that the average of the relative aerodynamic loss increase is  $\Omega = 0.39\%$  for all 50 cases as shown in Table 5. The minimum  $\Omega$  value is 0.23%. The first four film cooling holes are placed quite close to the suction side rim. This positioning makes them less effective in protecting the cavity surfaces from the heat because they directly join the leakage vortex from the suction side without creating a protective film layer on the cavity bottom surface. In addition, the coolant flow through the fifth hole, which is

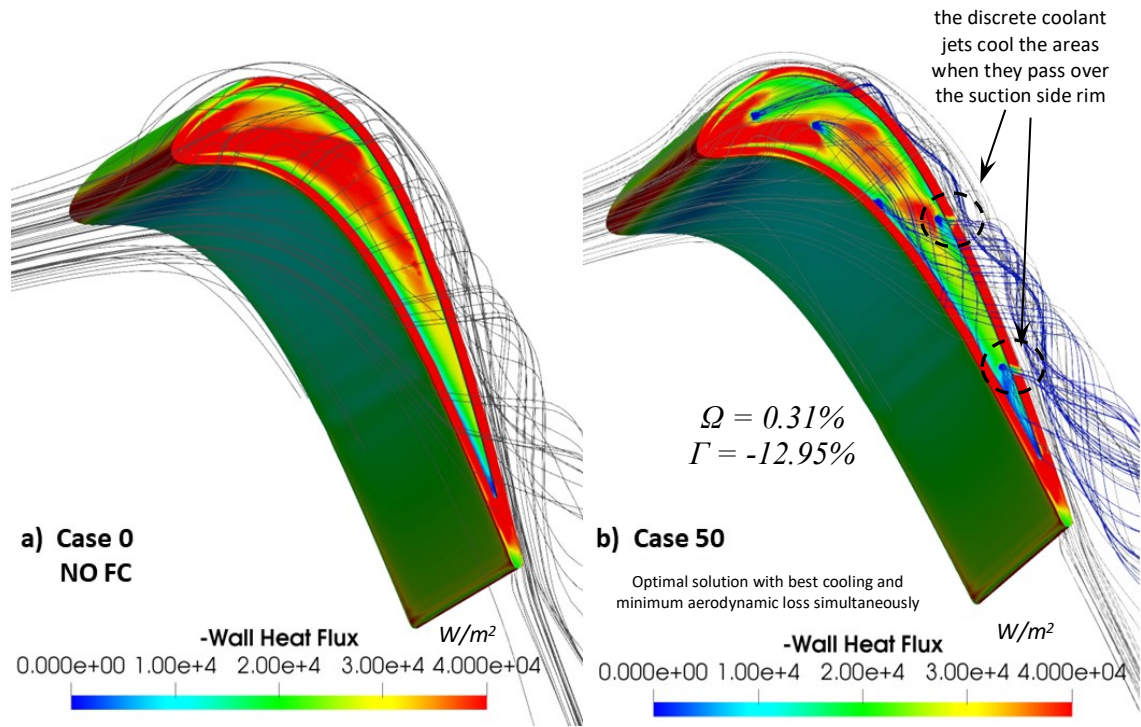
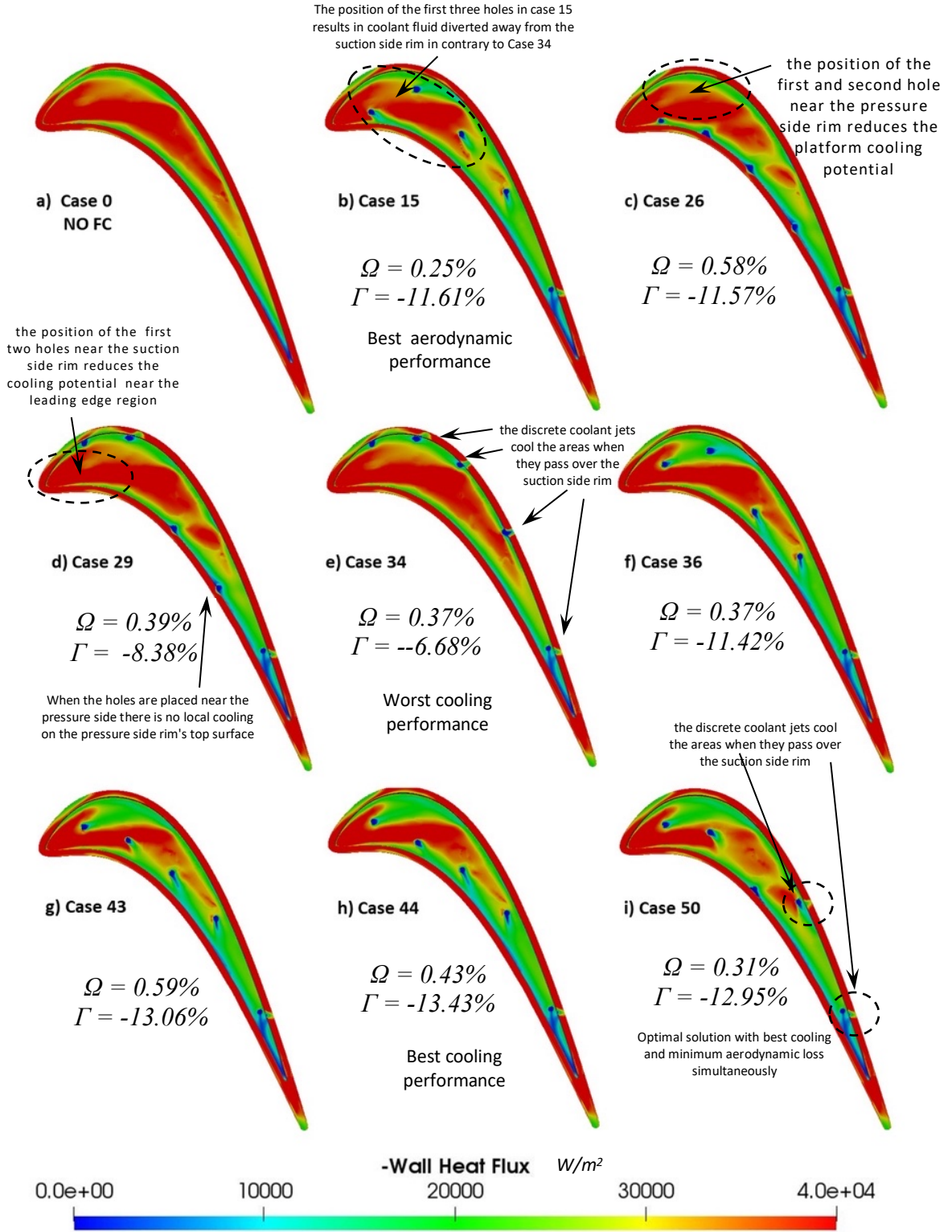


**Figure 15:** Wall heat flux [ $W/m^2$ ] on the blade and streamlines color-coded with temperature with STATIONARY casing,  $M=1.0$   
a) No film cooling case b) Case 50 (Optimum Case).

fixed, is divided into two parts. One part goes over the wedge area of the trailing edge, and the second part joins the leakage vortex by passing over the suction side rim. When all five cooling holes are located very near the suction side rim, they locally reduce the wall heat flux to the top surface of the rim, as indicated in Figure 16.(e). However, the platform cooling ability of this configuration is minimal.

**The worst aerodynamic penalty case:** Case 26 having all five cooling holes near the pressure side rim is one of the worst aerodynamic loss cases in this study because they are placed in the recirculation corner between the pressure side rim and the cavity platform. The aerodynamic loss character of this configuration is detrimental in producing one of the highest aerodynamic loss change values of  $\Omega = 0.58\%$ . The specific location of the first and second holes in Case 26 also reduces the cooling potential of the platform near the leading edge especially near the suction side rim. Even with



$$\Omega = \frac{\Delta C_{po,FC} - \Delta C_{po,NoFC}}{\Delta C_{po,NoFC}} \quad \Gamma = \frac{q_{total,FC} - q_{total,NoFC}}{q_{total,NoFC}}$$

**Figure 16:** Wall heat flux on the tip surface for eight selected film cooling cases with STATIONARY casing, M=1.0

the presence of two cooling holes the near leading edge area, the local heat flux levels are close to the non-cooled Case 0. The specific placement of the first two holes in Case 29 also leaves the near leading edge region without reasonable heat protection similar to Case 26.

**The case with minimum aerodynamic loss:** Case 15 shows the best aerodynamic performance with  $\Omega = 0.25\%$ . The passage of the coolant fluid over the suction side rim is reduced from the first four holes in contrary to Case 34 that has the worst cooling performance with  $\Gamma = -6.68\%$ . Early mixing of the coolant fluid with the tip leakage vortex outside the suction side rim is minimal for Case 15 that helps to achieve the best overall aerodynamic performance. Most of the coolant fluid is contained in the cavity before it was discharged near the trailing edge. The position of the first three holes in Case 15 results in coolant fluid diverted away from the suction side rim in contrary to Case 34.

### 4.3 *The effects of adding relative casing motion and lowering the blowing rate*

**The three best film cooling configurations with the lowest heat transfer:** These configurations were selected from Table 5 to investigate the effects of lower blowing ratio and imposed relative casing motion. The cases 18, 44 and 47 were re-computed at  $M=0.4$  and  $1.0$  by imposing the specific the relative motion of the casing in addition to their performance with a stationary casing. The speed of the relative motion (RM) was calculated from the rotational speed of the AFTRF at 1322 RPM, [49].

Table 6 displays the change in the total pressure coefficient  $\Delta C_{po}$  that is in reference to the non-cooled case for a stationary casing.  $C_{po}$  is in reference to the inlet plane value.  $\Delta C_{po}$  is calculated on the exit plane located at  $x = 1.25C_x$  downstream from the airfoil's trailing edge. The best-cooled cases with stationary casing are used as reference cases for the cases that have casing relative motion. Aerodynamic loss and cooled total heat flux values for the cases 18, 44 and 47 as shown in Table 6 are very close to each other for the blowing rate  $M=1.0$ . These best three cooling arrangements represent the hole placements very near the camberline of the airfoil as shown in Fig.17.(a). The hole placements for each case are slightly different from each other. They are used in documenting the aerodynamic penalty and cooling performance changes for the reduced blowing rate of  $0.4$  and imposed casing motion.

**Influence of reducing the blowing rate from  $M=1.0$  to  $M=0.4$ , STATIONARY casing :** A typical film cooling blowing rate range in present day gas turbine applications vary from  $M=0.4$  to  $1.0$ . Therefore, the tip heat transfer and aerodynamic loss computations for the cases 18, 44 and 47 for  $M=0.4$  are also performed with a stationary casing as shown in Figure17.(b). Table 7 summarizes the main results of this analysis. The relative change of the aerodynamic losses  $\Omega_M$  and wall heat flux  $\Gamma_M$  in reference to  $M=1.0$  case are defined in Table 7.

**Table 6:** Aerodynamic loss  $\Delta C_{po}$  and total heat flux  $q_{total}$  for three best film cooling cases  $M=1$ , with STATIONARY casing.

Case # (i)	$\Delta C_{po}$	—	$q_{cavity}$ [W]	$q_{tip}$ [W]	$q_{side}$ [W]	$q_{total}$ [W]	—
18	-0.21752	----	-31.84	-29.61	-11.46	-72.91	----
44	-0.21756	----	-31.45	-29.71	-11.65	-72.81	----
47	-0.21744	----	-31.42	-29.74	-11.77	-72.94	----

**Table 7:** Influence of reducing the blowing rate from  $M=1.0$  to  $M=0.4$ , with STATIONARY casing.

$$\Omega_M = \frac{\Delta C_{po,FC,M=0.4} - \Delta C_{po,FC,M=1.0}}{\Delta C_{po,FC,M=1.0}} \quad \Gamma_M = \frac{q_{total,FC,M=0.4} - q_{total,FC,M=1.0}}{q_{total,FC,M=1.0}}$$

Case # (i)	$\Delta C_{po}$	$\Omega_M$	$q_{cavity}$ [W]	$q_{tip}$ [W]	$q_{side}$ [W]	$q_{total}$ [W]	$\Gamma_M$
18	-0.21783	<b>0.14%</b>	-34.24	-30.50	-12.25	-76.98	<b>5.58%</b>
44	-0.21745	<b>-0.05%</b>	-34.35	-31.04	-12.61	-78.00	<b>7.13%</b>
47	-0.21740	<b>-0.02%</b>	-34.21	-31.06	-12.68	-77.96	<b>6.88%</b>

**Table 8:** Influence of adding the casing relative motion  $RM$ , blowing rate  $M=1.0$ .

$$\Omega_{RM} = \frac{\Delta C_{po,FC,M=1.0,RM} - \Delta C_{po,FC,M=1.0}}{\Delta C_{po,FC,M=1.0}} \quad \Gamma_{RM} = \frac{q_{total,FC,M=1.0,RM} - q_{total,FC,M=1.0}}{q_{total,FC,M=1.0}}$$

Case # (i)	$\Delta C_{po}$	$\Omega_{RM}$	$q_{cavity}$ [W]	$q_{tip}$ [W]	$q_{side}$ [W]	$q_{total}$ [W]	$\Gamma_{RM}$
18	-0.23576	<b>8.39%</b>	-25.39	-28.80	-10.08	-64.28	<b>-11.85%</b>
44	-0.23565	<b>8.31%</b>	-26.51	-28.93	-10.50	-65.94	<b>-9.44%</b>
47	-0.23563	<b>8.36%</b>	-26.67	-28.88	-10.50	-66.05	<b>-9.44%</b>

**Table 9:** Influence of adding the casing relative motion  $RM$ , blowing rate  $M=0.4$ .

$$\Omega_{RM} = \frac{\Delta C_{po,FC,M=0.4,RM} - \Delta C_{po,FC,M=0.4}}{\Delta C_{po,FC,M=0.4}} \quad \Gamma_{RM} = \frac{q_{total,FC,M=0.4,RM} - q_{total,FC,M=0.4}}{q_{total,FC,M=0.4}}$$

Case # (j)	$\Delta C_{po}$	$\Omega_{RM}$	$q_{cavity}$ [W]	$q_{tip}$ [W]	$q_{side}$ [W]	$q_{total}$ [W]	$\Gamma_{RM}$
18	-0.23517	<b>7.96%</b>	-26.64	-30.14	-11.09	-67.88	<b>-11.82%</b>
44	-0.23519	<b>8.16%</b>	-27.15	-30.11	-11.22	-68.48	<b>-12.21%</b>
47	-0.23519	<b>8.18%</b>	-27.24	-30.10	-11.22	-68.55	<b>-12.07%</b>

Total heat flux to the tip surfaces measurably increased by about  $\Gamma_M = 6.5\%$  on the average when the blowing rate is reduced to  $M=0.4$ . The aerodynamic loss levels were very slightly influenced when  $M$  is reduced to  $0.4$ . The aerodynamic loss level change  $\Omega_M$  for each one of the cases was less than  $0.15\%$ .

**Influence of adding the CASING RELATIVE MOTION at the blowing rate  $M=1.0$  :** Fig.17.(c) shows the tip heat transfer distribution for  $M=1$  when the relative motion of the casing is included in the computations. The details of this case with casing relative motion (RM) are presented in Table 8. The relative changes of the aerodynamic loss  $\Omega_{RM}$  and total heat flux  $\Gamma_{RM}$  are defined in Table 8.

The aerodynamic loss coefficient is measurably elevated by the addition of casing relative motion.  $\Omega_{RM}$  increases by  $+8.3\%$  on the average for all three cases when compared to the computations with a stationary wall. The relative motion of the outer casing against the tip leakage flow and the cavity cooling jets results in a complex shear flow between the casing and cavity flow. The leakage flow is sheared in opposite direction by the relative motion of the casing just over the cavity. This counteracting shear flow reduces the mass flow rate of the tip leakage flow. However the aerodynamic losses induced in the cavity are encouraged when compared to the stationary casing case. Imposing the casing relative motion is extremely beneficial as far as the cooling of the tip surfaces is concerned. Figure 17.(c) indicates that a total heat flux reduction of  $\Gamma_{RM} = -10.2\%$  is possible, as the average of all three configurations, Table 8. The casing relative motion results presented in Fig.17.(c) show the important local heat flux reductions on the cavity floor as indicated by wider green-blue areas when compared to Fig.17.(a). This observation is consistent with that of Sakaoglu and Kahveci [15].

**Influence of adding the CASING RELATIVE MOTION at the blowing rate  $M=0.4$  :** Table 9 and Fig.17(d) provide the details of the aerodynamic loss and heat transfer characteristics for the cooling configurations Case 18, 44 and 47 for  $M=0.4$ . The results at this reduced blowing rate were obtained by taking casing relative motion into account. The definitions of the relative changes of the aerodynamic loss  $\Omega_{RM}$  and total heat flux  $\Gamma_{RM}$  with respect to the stationary casing case are included in Table 9.

The aerodynamic loss change result with the casing relative motion is about  $\Omega_{RM} = +8.1\%$  (on the average) higher than the case with a stationary casing as shown in Fig.17.(d). The aerodynamic loss change  $\Omega_{RM} = +8.1\%$  for  $M=0.4$  is slightly less than the change  $\Omega_{RM} = +8.35\%$  for  $M=1.0$ . Adding the relative motion of the casing consistently increases the aerodynamic penalty at the same blowing rate. A total heat flux reduction to the tip for  $M=0.4$  case is  $\Gamma_{RM} = -12.03\%$  with casing motion, as shown in Table 9. Including casing relative motion in the analysis consistently results in much better cooled cavity platform surfaces in the current range of blowing rates.



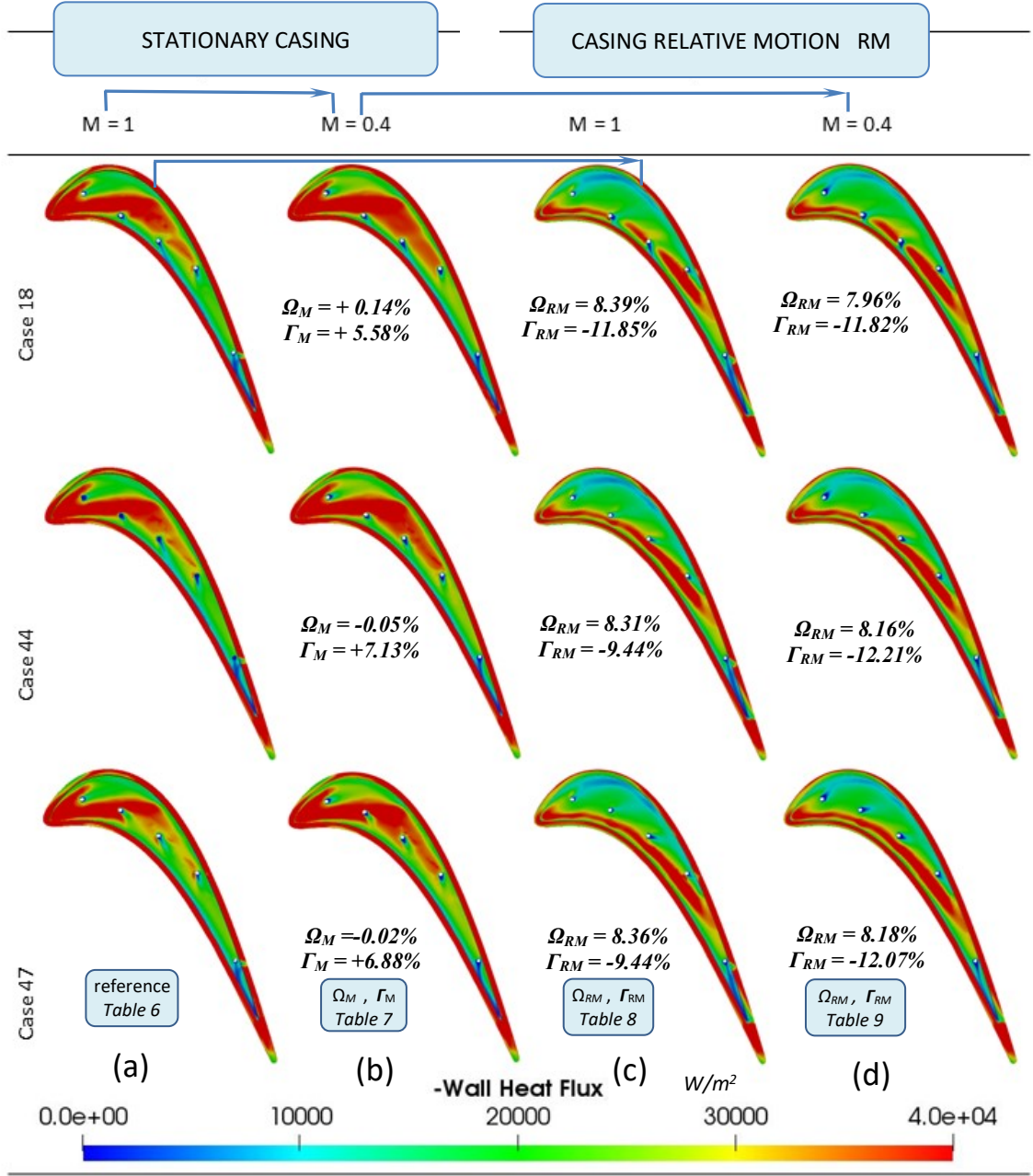


**Figure 17:** A comparison of total heat flux on the tip surfaces without and with casing relative motion RM, for both blowing rates of  $M=0.4$  and  $M=1.0$ .

**Aerodynamic loss mechanisms at the mid-chord location:** Figure 18 shows a comparison of aerodynamic losses at airfoil mid-chord location ( $x = 0.47C_x$ ) in a plane normal to the cavity platform without and with casing relative motion, for  $M=1.0$ . Fig.18.a shows a distinct tip vortex in the mainstream at the suction side rim for the stationary casing. The core of this vortical flow has the highest level of aerodynamic loss as shown by the dark blue area. The tip vortex rotates in the clockwise direction and it strongly counteracts the passage vortex dissipating its mean kinetic energy and containing it to a narrow area. The location of the passage vortex is between 0.8 and 0.9 normalized span as shown in Fig.18.(a) and 19. Although the passage vortex loss peak at 85% span is



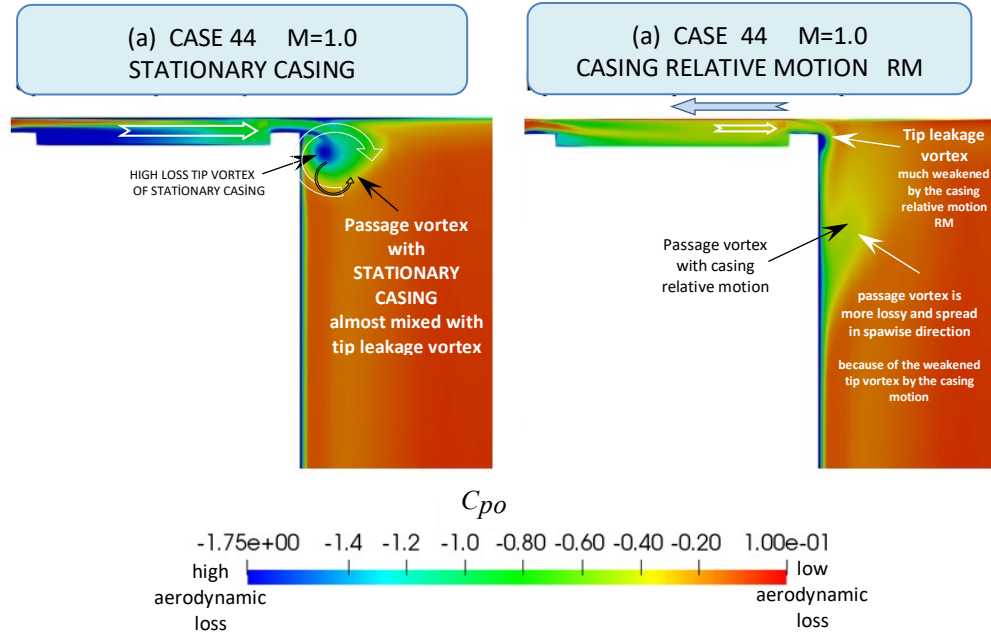


**Figure 18:** Total pressure coefficient  $C_{po}$  on the section at  $x = 0.47C_x$   
a) Case 44,  $M = 1.0$ , STATIONARY casing    b) Case 44,  $M = 1.0$ , casing relative motion, RM.

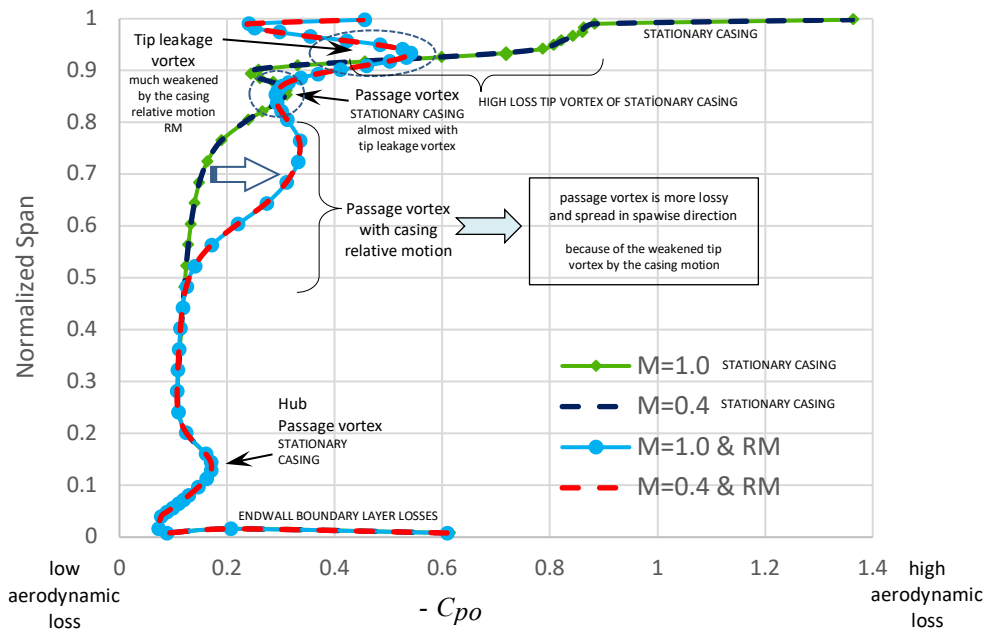


**Figure 19:** Spanwise distribution of negative of total pressure loss coefficient,  $\left(-\frac{\int \rho u C_{po} dz}{\int \rho u dz}\right)$ , at  $x=1.25C_x$ .

$C_{po} = -0.3$ , the losses caused by the tip leakage vortex are between  $C_{po} = -0.35$  and  $-1.3$  when the casing is stationary. The endwall boundary layer losses are significant in a very narrow span between 97% and the casing. The same is true for the hub endwall boundary layer.

When the casing relative motion is taken into account, the tip leakage flow is sheared in opposite direction by the relative motion of the casing over the cavity. This counteracting and strong shear flow reduces the mass flow of the tip leakage flow. The tip leakage vortex is much weakened by the turbulent shear imposed by the casing motion as shown in Fig.18.(b) and Fig.19. An important result of the weakening of the tip vortex is that the upper passage vortex becomes more dominant, lossy and spread in the spanwise direction when the casing motion is imposed, Fig.19. The passage vortex covers a wider span from 50% to 85% and the aerodynamic losses are almost doubled. An average aerodynamic loss increase of  $\mathcal{Q}_{RM} = +8.35\%$  (on the average) is observed because of the imposed casing motion as shown in Figure17.(c). This loss enhancement is mainly due to the significant spreading of a more lossy passage vortex between 50% span to 85.

The casing relative motion pushes the maistream tip leakage vortex to the suction side and it decreases tip leakage flow rate. It also reduces the cavity flow recirculation and increases local total pressure in the cavity especially near the pressure side rim. As a result less maistream gases leak into the cavity from the pressure side rim. However, the casing motion promotes the pasage vortex in its effort to increase overall aerodynamic losses measured in the exit plane at  $x=1.25C_x$ , by weakening the tip vortex in the passage.

## 5. Conclusions

This study presents a time-efficient computational optimization method for the film-cooled squealer tip of a high-pressure turbine blade for its aerothermal performance. The influence of film cooling hole positions, blowing rates and imposing the relative motion of the casing are investigated. A non-linear optimization method as a genetic algorithm is adequate to determine the optimum positions of film cooling holes in such a complex and three-dimensional flow environment. Hole positions are optimized for heat transfer and total pressure loss on the tip surfaces. In order not to update the mesh every time the hole positions change, an automatic grid updating feature with densification on the lines where the positions of film cooling hole optimized is used. The automatic grid updating approach provides considerable computational time savings. The significant findings are as follows:

### OPTIMIZATION OF 50 FILM COOLING ARRANGEMENTS (STATIONARY CASING, $M=1.0$ )

- The best tip cooling performance is obtained when the holes are at the camberline or near the camberline, Case 44.
- Five discrete cooling holes located near the camberline may have all viable cooling performances with heat flux reduction  $\Gamma$  better than 11%. Moving them toward the pressure side rim tends to gradually increase the aerodynamic losses, as observed in Cases 15, 36, 43 and 44. The holes pushed toward the pressure side rim are good candidates to weaken the tip leakage resulting in a passage vortex with stronger loss generation at the passage

exit.

- Positioning the first two holes too close to the suction or pressure side rim, reduces the platform cooling potential near the leading edge region (Case 29 & Case 26).
- The worst tip cooling performance occurs when all holes are kept near the suction side rim for Case 34. This positioning makes them less effective in protecting the surfaces from the heat because they immediately join the leakage vortex from the suction side without creating a protective film layer on the cavity bottom surface.
- Case 26, having all five film cooling holes near the pressure side rim is one of this study's worst aerodynamic loss cases in this study because they are placed in the recirculation corner between the pressure side rim and the cavity platform. The normal jets from the holes located near the pressure side rim (Cases 26 and 43) help to reduce the strength of the tip leakage flow in the passage. A weakened tip vortex results in a highly-spread passage vortex, generating a high aerodynamic loss. However, these two hole arrangements have very good platform cooling ability.
- The top surfaces of the the cavity rims are typically high heat transfer areas. However, the discrete coolant jets cool the areas locally as they pass over the suction side rim, especially for the third and fourth coolant jets. When the holes are placed near the pressure side or the camberline, there is no local cooling for the top surface of the pressure side rim.
- When all five cooling holes are located very near the suction side rim, they effectively reduce the local wall heat flux along their trajectory on the top surface of the rim.

#### REDUCING THE BLOWING RATE TO 0.4 (STATIONARY CASING)

- The aerodynamic loss levels are very slightly influenced when  $M$  is reduced to 0.4. The influence of film cooling injection from the five discrete holes in each passage is not strongly felt in the total pressure field at the exit. This slight change in  $C_{po}$  is mainly because of the small amount of the coolant mass flow rate compared to that of the mainstream and mixing occurring down to the exit plane  $x/C_x=1.25$ . The aerodynamic loss level change  $\Omega_M$  is less than 0.15 % for all cases with the best cooling performance.
- Total heat flux to the tip surfaces measurably increased by about  $\Gamma_M = +6.5\%$  on average when the blowing rate is reduced to  $M=0.4$ , suggesting slightly less effective cooling.

#### IMPOSING THE CASING RELATIVE MOTION

- The addition of casing relative motion measurably increases the aerodynamic loss coefficient.  $\Omega_{RM}$  increases by 8.3% on average for all three 'best-cooling cases' when compared to the computations with a stationary wall for  $M=1.0$ . Imposing the casing relative motion in the analysis, a total heat flux reduction of  $\Gamma_{RM} = -10.2\%$  is possible, as the average of all three configurations.
- When the blowing rate is reduced to  $M=0.4$ , the aerodynamic loss with casing motion is about  $\Omega_{RM} = +8.1\%$  (on average) for all three cases. This value is slightly lower than the change  $\Omega_{RM} = +8.35\%$  for  $M=1.0$ . Adding the relative motion of the casing increases the aerodynamic penalty at the same blowing rate.
- A total heat flux reduction to the tip for the  $M=0.4$  case is  $\Gamma_{RM} = -12.03\%$  with casing motion, as shown in Table 9. Including the casing relative motion in the analysis consistently results in much better cooled cavity platform surfaces for both blowing rates.
- The casing relative motion pushes the tip leakage vortex in the mainstream to the suction side, and decreasing the tip leakage flow rate. It also reduces the cavity flow recirculation and increases local total pressure

, especially near the pressure side rim. As a result, less mainstream gas leaks into the cavity weakening the tip leakage vortex.

- The tip leakage flow is sheared in the opposite direction by the motion of the casing over the cavity. An important result of the weakening of the tip vortex is that the upper passage vortex becomes more dominant, lossy and spread in the spanwise direction when the casing motion is imposed.

- An average aerodynamic loss increase of  $\Omega_{RM} = +8.35\%$  occurs because of the casing motion. The passage vortex covers a much wider span from 50% to 85%, and the losses are almost doubled in its coverage area. This loss enhancement is mainly due to the significant spreading of the passage vortex between 50% span to 85.

- The optimum positions of film cooling holes depend on the characteristics of tip leakage flow. These positions change with respect to the geometry, boundary conditions of the flow and the specific blade profile. Hence, the cooling effectiveness can be improved by employing the particular position optimization method presented in this investigation.

- This investigation also shows that including the relative motion of the casing in the computations strongly influences the heat transfer rates to the squealer tip region of an HP turbine blade. Therefore, experimental and computational heat transfer studies in the tip region of turbine blades need to consider the relative motion of the blade tip against a stationary casing.

## References

- [1] Han, J. C., Dutta, S., & Ekkad, S. (2012). Gas turbine heat transfer and cooling technology. CRC Press, ISBN 9781439855683.
- [2] Saha, A. K., Acharya, S., Bunker, R., & Prakash, C. (2006). Blade tip leakage flow and heat transfer with pressure-side winglet. *International Journal of Rotating Machinery*, 2006. doi:10.1155/IJRM/2006/17079.
- [3] Azad, G. S., Han, J. C., Bunker, R. S., & Lee, C. P. (2002). Effect of squealer geometry arrangement on a gas turbine blade tip heat transfer. *J. Heat Transfer*, 124(3), 452-459. doi:10.1115/1.1471523.
- [4] Acharya, S., Yang, H., Ekkad, S. V., Prakash, C., & Bunker, R. (2002, January). Numerical simulation of film cooling on the tip of a gas turbine blade. In *Turbo Expo: Power for Land, Sea, and Air* (Vol. 36088, pp. 1051-1062). doi:10.1115/gt2002-30553.
- [5] Key, N. L., & Arts, T. (2006). Comparison of turbine tip leakage flow for flat tip and squealer tip geometries at high-speed conditions. *Journal of Turbomachinery*, 128 (2) 213–220. doi:10.1115/1.2162183.
- [6] Schabowski, Z., Hodson, H., Giacche, D., Power, B., & Stokes, M. R. (2014). Aeromechanical optimization of a winglet-squealer tip for an axial turbine. *Journal of Turbomachinery*, 136(7), 071004. doi:10.1115/1.4025687.
- [7] Dey, D., & Camci, C. (2001, June). Aerodynamic tip desensitization of an axial turbine rotor using tip platform extensions. In *Turbo Expo: Power for Land, Sea, and Air* (Vol. 78507, p. V001T03A069). ASME. doi:10.1115/2001-GT-0484.
- [8] Ledezma, G. A., Allen, J., & Bunker, R. S. (2013, September). An experimental and numerical investigation into the effects of squealer blade tip modifications on aerodynamic performance. In *ASME Turbine Blade Tip Symposium* (Vol. 56079, p. V001T03A002). American Society of Mechanical

- Engineers. doi:10.1115/TBTS2013-2004.
- [9] Yan, X., Huang, Y., & He, K. (2017). Investigations into heat transfer and film cooling effect on a squealer-winglet blade tip. *International Journal of Heat and Mass Transfer*, 115, 955-978. doi:10.1016/j.ijheatmasstransfer.2017.08.090.
  - [10] Du, K., Li, Z., Li, J., & Sunden, B. (2019). Influences of a multi-cavity tip on the blade tip and the over tip casing aerothermal performance in a high pressure turbine cascade. *Applied Thermal Engineering*, 147, 347-360. doi:10.1016/j.applthermaleng.2018.10.093.
  - [11] Jiang, S., Li, Z., & Li, J. (2019). Effects of the squealer winglet structures on the heat transfer characteristics and aerodynamic performance of turbine blade tip. *International Journal of Heat and Mass Transfer*, 139, 860-872. doi:10.1016/j.ijheatmasstransfer.2019.05.064.
  - [12] Zhou, Z., Chen, S., Li, W., & Wang, S. (2019). Thermal performance of blade tip and casing coolant injection on a turbine blade with cavity and winglet-cavity tip. *International Journal of Heat and Mass Transfer*, 130, 585-602. doi:10.1016/j.ijheatmasstransfer.2018.10.130.
  - [13] Yan, X., Yu, J., Ye, M., & He, K. (2023). Reduction of heat transfer and improvement of film cooling effect on squealer tip with multi-rib design concept. *Journal of Mechanical Science and Technology*, 1-14. <https://doi.org/10.1007/s12206-023-0751-8>
  - [14] Wang, J., Sundén, B., Zeng, M., & Wang, Q. W. (2012). Influence of different rim widths and blowing ratios on film cooling characteristics for a blade tip. *Journal of heat transfer*, 134(6). doi:10.1115/1.4006017.
  - [15] Sakaoglu, S., & Kahveci, H. S. (2019). Effect of cavity depth on thermal performance of a cooled blade tip under rotation. *International Journal of Heat and Mass Transfer*, 143, 118561. doi:10.1016/j.ijheatmasstransfer.2019.118561.
  - [16] Eriksen, V. L., & Goldstein, R. J. (1974). Heat transfer and film cooling following injection through inclined circular tubes. *Journal of heat transfer*, 96(2): 239-245. doi:10.1115/1.3450171.
  - [17] Yan, X., Huang, Y., & He, K. (2018). Effect of ejection angle and blowing ratio on heat transfer and film cooling effect on a winglet tip. *International Journal of Heat and Mass Transfer*, 125, 357-374. doi:10.1016/j.ijheatmasstransfer.2018.04.097.
  - [18] Kim, Y. W., & Metzger, D. E. (1995). Heat transfer and effectiveness on film cooled turbine blade tip models. *Journal of Turbomachinery*, 117(1): 12-21. doi:10.1115/1.2835630.
  - [19] Cunliang, L. I. U., Zhang, F., Zhang, S., Qingqing, S. H. I., & Hui, S. O. N. G. (2022). Experimental investigation of the full coverage film cooling effectiveness of a turbine blade with shaped holes. *Chinese Journal of Aeronautics*, 35(3), 297-308. <https://doi.org/10.1016/j.cja.2021.06.022>
  - [20] Wang, C., Zhang, J., & Zhou, J. (2016). Optimization of a fan-shaped hole to improve film cooling performance by RBF neural network and genetic algorithm. *Aerospace Science and Technology*, 58, 18-25. <https://doi.org/10.1016/j.ast.2016.08.004>
  - [21] Zhang, B. L., Zhu, H. R., Yao, C. Y., Liu, C. L., & Zhang, Z. (2021). Investigation on film cooling and aerodynamic performance of blade tip with tangential jet cooling scheme at transonic flow. *Aerospace Science and Technology*, 118, 107067. <https://doi.org/10.1016/j.ast.2021.107067>
  - [22] Cho, H. H., & Goldstein, R. J. (1995). Heat (mass) transfer and film cooling effectiveness with injection through discrete holes: Part II—On the exposed surface. *Journal of Turbomachinery*, 117(3): 451-460. doi:10.1115/1.2835681.

- [23] Rezasoltani, M., Lu, K., Schobeiri, M. T., & Han, J. C. (2015). A combined experimental and numerical study of the turbine blade tip film cooling effectiveness under rotation condition. *Journal of Turbomachinery*, 137(5), 051009. doi:10.1115/GT2014-25625.
- [24] Wang, J., Sundén, B., Zeng, M., & Wang, Q. (2015). Film cooling effects on the tip flow characteristics of a gas turbine blade. *Propulsion and Power Research*, 4(1), 9-22. doi:10.1016/j.jprr.2015.02.003.
- [25] Rao, N. M., & Camci, C. (2004). Axial turbine tip desensitization by injection from a tip trench: Part 2—leakage flow sensitivity to injection location. In *Turbo Expo: Power for Land, Sea, and Air* (Vol. 41707, pp. 1089-1098). doi:10.1115/GT2004-53258.
- [26] Cheng, F. N., Zhang, J. Z., Chang, H. P., & Zhang, J. Y. (2018). Investigations of film-cooling effectiveness on the squealer tip with various film-hole configurations in a linear cascade. *International Journal of Heat and Mass Transfer*, 117, 344-357. doi:10.1016/j.ijheatmasstransfer.2017.09.100.
- [27] Yang, H., Chen, H. C., & Han, J. C. (2004, January). Numerical prediction of film cooling and heat transfer with different film-hole arrangements on the plane and squealer tip of a gas turbine blade. In *Turbo Expo: Power for Land, Sea, and Air* (Vol. 41685, pp. 177-187). doi:10.1115/GT2004-53199.
- [28] Ahn, J., Mhetras, S., & Han, J. C. (2005). Film-cooling effectiveness on a gas turbine blade tip using pressure-sensitive paint. *J. Heat Transfer*, 127(5), 521-530. doi:10.1115/1.1909208.
- [29] He, K. (2017). Investigations of film cooling and heat transfer on a turbine blade squealer tip. *Applied Thermal Engineering*, 110, 630-647. doi:10.1016/j.applthermaleng.2016.08.173.
- [30] Tong, F., Gou, W., Li, L., Liu, Q., Yue, Z., & Xie, G. (2015). Investigation on heat transfer of a rotor blade tip with various film cooling holes arrangements and groove depths. *Advances in Mechanical Engineering*, 7(2), 1687814014568499. <https://doi.org/10.1177/1687814014568499>
- [31] Park, J. S., Lee, D. H., Rhee, D. H., Kang, S. H., & Cho, H. H. (2014). Heat transfer and film cooling effectiveness on the squealer tip of a turbine blade. *Energy*, 72, 331-343. doi:10.1016/j.energy.2014.05.041.
- [32] Wang, Y., Song, Y., Yu, J., & Chen, F. (2019). Effect of the injection orientation and position on the leakage flow in a honeycomb-tip turbine cascade. *International Journal of Heat and Mass Transfer*, 144, 118633. doi:10.1016/j.ijheatmasstransfer.2019.118633.
- [33] Senel, C. B., Maral, H., Kavurmacioglu, L. A., & Camci, C. (2018). An aerothermal study of the influence of squealer width and height near a HP turbine blade. *International Journal of Heat and Mass Transfer*, 120, 18-32. doi:10.1016/j.ijheatmasstransfer.2017.12.017.
- [34] Yıldız, F. (2019). Position Optimization of Film Cooling Holes on a Squealer Turbine Blade Tip (Master's Thesis, Marmara Univesity (Turkey)). 28243114.
- [35] Wilcox, D. C. (1993). Comparison of two-equation turbulence models for boundary layers with pressure gradient. *AIAA Journal*, 31(8), 1414-1421. doi:10.2514/3.11790.
- [36] Menter, F. R. (1994). Two-equation eddy-viscosity turbulence models for engineering applications. *AIAA Journal*, 32(8), 1598-1605. doi:10.2514/3.12149.
- [37] OpenFOAM®, <https://openfoam.org/>, accessed: 31-07-2021.
- [38] Dozić, D. J., & Urošević, B. D. G. (2019). Application of artificial neural networks for testing long-term energy policy targets. *Energy*, 174, 488-496. doi:10.1016/j.energy.2019.02.191.
- [39] Poort, J. P., Ramdin, M., van Kranendonk, J., & Vlugt, T. J. (2019). Solving vapor-liquid flash problems using artificial neural networks. *Fluid Phase Equilibria*, 490, 39-47. doi:10.1016/j.fluid.2019.02.023.

- [40] Taheri, M. H., Abbasi, M., & Jamei, M. K. (2019). Using artificial neural network for computing the development length of MHD channel flows. *Mechanics Research Communications*, 99, 8-14. doi:10.1016/j.mechrescom.2019.06.003.
- [41] Deveci, K., Maral, H., Senel, C. B., Alpman, E., Kavurmacioglu, L., & Camci, C. (2018). Aerothermal optimization of squealer geometry in axial flow turbines using genetic algorithm. *Journal of Thermal Engineering*, 4(3), 1896-1911.
- [42] Maral, H., Alpman, E., Kavurmacioğlu, L., & Camci, C. (2019). A genetic algorithm based aerothermal optimization of tip carving for an axial turbine blade. *International Journal of Heat and Mass Transfer*, 143, 118419. doi: 10.1016/j.ijheatmasstransfer.2019.07.069.
- [43] Maral, H., Şenel, C. B., Deveci, K., Alpman, E., Kavurmacioğlu, L., & Camci, C. (2020). A genetic algorithm based multi-objective optimization of squealer tip geometry in axial flow turbines: a constant tip gap approach. *Journal of Fluids Engineering*, 142(2). doi:10.1115/1.4044721.
- [44] Octave, <https://www.gnu.org/software/octave/>, accessed: 22- 01-2020.
- [45] Deb, K., Pratap, A., Agarwal, S., & Meyarivan, T. A. M. T. (2002). A fast and elitist multi-objective genetic algorithm: NSGA-II. *IEEE transactions on evolutionary computation*, 6(2), 182-197. doi:10.1109/4235.996017.
- [46] Camara, M. V. O., Ribeiro, G. M., & Tosta, M. D. C. R. (2018). A Pareto optimal study for the multi-objective oil platform location problem with NSGA-II. *Journal of Petroleum Science and Engineering*, 169, 258-268. doi:10.1016/j.petrol.2018.05.037.
- [47] Han, H., Yu, R., Li, B., & Zhang, Y. (2019). Multi-objective optimization of corrugated tube inserted with multi-channel twisted tape using RSM and NSGA-II. *Applied Thermal Engineering*, 159, 113731. doi:10.1016/j.applthermaleng.2019.113731.
- [48] Vo-Duy, T., Duong-Gia, D., Ho-Huu, V., Vu-Do, H. C., & Nguyen-Thoi, T. (2017). Multi-objective optimization of laminated composite beam structures using NSGA-II algorithm. *Composite Structures*, 168, 498-509. doi:10.1016/j.compstruct.2017.02.038.
- [49] Camci, C. (2004). A turbine research facility to study tip desensitization including cooling flows. *VKI Lecture Series on "Turbine Blade Tip Design and Tip Clearance Treatment*, 1-26. ISBN 2-930389-51-6, Brussels,Belgium.
- [50] Turgut, Ö. H., & Camci, C. (2016). Factors influencing computational predictability of aerodynamic losses in a turbine nozzle guide vane flow. *Journal of Fluids Engineering*, 138(5). doi:10.1115/1.4031879.
- [51] McLean, C., Camci, C., & Glezer, B. (2001). Mainstream aerodynamic effects due to wheel-space coolant injection in a high-pressure turbine stage: Part I—Aerodynamic measurements in the stationary frame. *J. Turbomach.*, 123(4), 687-696. doi:10.1115/1.1401026.
- [52] Beer, W. (2008). Optimization of a compound lean turbine blade in a linear cascade. (Doctoral dissertation, Technischen Universität Wien (Austria)).
- [53] Klaput, T. (1996). Control of Near Wall Flow on an Isolated Airfoil at High Angle of Attack Using Piezoelectric Surface Vibration Elements. (Master's Thesis, Pennsylvania State University (USA)).
- [54] Somers, D. M., & Maughmer, M. D. (1990). The SM701 Airfoil. Airfoils, Inc., December.
- [55] Somers, D., & Maughmer, M. D. (1992). The SM701 Airfoil: An airfoil for world-class sailplanes. *Technical Soaring*, 16(3), 70-77.
- [56] Langtry, R. B., & Menter, F. R. (2009). Correlation-based transition modeling for unstructured

parallelized computational fluid dynamics codes. *AIAA Journal*, 47(12), 2894-2906. [doi:10.2514/1.42362](https://doi.org/10.2514/1.42362).

- [57] Helton, J. C., & Davis, F. J. (2003). Latin hypercube sampling and the propagation of uncertainty in analyses of complex systems. *Reliability Engineering & System Safety*, 81(1), 23-69. doi:10.1016/S0951-8320(03)00058

**Appendix – I: Coordinates of tip airfoil section of AFTRF at Penn State [44]**

x-Coordinate [mm]	y-Coordinate [mm]	x-Coordinate [mm]	y-Coordinate [mm]
-1.512	1.906	29.33	-23.823
-4.31	4.462	30.965	-28.265
-7.173	6.741	32.506	-32.569
-10.096	8.716	33.952	-36.731
-13.076	10.349	35.318	-40.749
-16.089	11.609	36.606	-44.62
-19.099	12.49	37.823	-48.344
-22.058	13.015	38.971	-51.919
-24.794	13.232	40.005	-55.187
-27.277	13.263	40.931	-58.146
-29.497	13.188	41.752	-60.797
-31.452	13.056	42.47	-63.137
-33.145	12.919	43.089	-65.167
-34.58	12.833	43.61	-66.885
-35.808	12.826	44.053	-68.353
-36.838	12.905	44.43	-69.587
-37.673	13.059	44.744	-70.605
-38.322	13.261	44.968	-71.42
-38.792	13.489	45.062	-72.063
-39.115	13.711	44.966	-72.539
-39.358	13.93	44.739	-72.878
-39.526	14.13	44.492	-73.091
-39.637	14.292	44.274	-73.203
-39.752	14.508	44.086	-73.258
-39.869	14.813	43.827	-73.292
-39.953	15.212	43.503	-73.251
-39.982	15.701	43.16	-73.102
-39.921	16.351	42.808	-72.725
-39.721	17.175	42.452	-72.129
-39.355	18.171	42.085	-71.364
-38.784	19.327	41.697	-70.593
-38.004	20.649	41.105	-69.326
-36.987	22.128	40.48	-68.032
-35.701	23.816	39.741	-66.503
-34.102	25.67	38.886	-64.739
-32.14	27.632	37.915	-62.741
-29.729	29.584	36.828	-60.509
-26.81	31.38	35.617	-58.044
-23.339	32.808	34.294	-55.348
-19.512	33.645	32.901	-52.538
-15.434	33.811	31.44	-49.616
-11.229	33.241	29.908	-46.584
-7.031	31.901	28.301	-43.443
-2.982	29.781	26.616	-40.196
0.816	26.956	24.845	-36.845
4.341	23.558	22.986	-33.394
7.508	19.823	21.092	-29.692
10.379	15.856	19.159	-26.552
13.025	11.736	17.176	-23.17
15.479	7.499	15.139	-19.889
17.772	3.172	13.038	-16.508
19.925	-1.226	10.878	-13.241
21.923	-5.674	8.623	-10.034
23.922	-10.166	6.276	-6.894
25.791	-14.692	3.813	-3.844
27.59	-19.246	1.224	-0.9



**Appendix – II:** Coordinates of SM701 Airfoil [49], [50]

Upper Surface		Lower Surface	
x/c	y/c	x/c	y/c
0.00168	0.00771	0.00016	-0.0021
0.00736	0.0191	0.00435	-0.0098
0.01701	0.03121	0.01501	-0.0163
0.03055	0.04344	0.03127	-0.0224
0.04794	0.05534	0.05277	-0.028
0.06915	0.06648	0.07923	-0.0329
0.09417	0.07658	0.11036	-0.0373
0.12295	0.08544	0.14575	-0.041
0.15541	0.09296	0.18488	-0.0442
0.19133	0.09914	0.22722	-0.0467
0.23041	0.10397	0.27222	-0.0485
0.27229	0.10746	0.31929	-0.0494
0.31654	0.10964	0.36784	-0.0494
0.36268	0.11055	0.41726	-0.048
0.41019	0.11018	0.46727	-0.0449
0.45853	0.10853	0.51811	-0.0398
0.50714	0.10557	0.56979	-0.0334
0.55548	0.1012	0.62191	-0.0262
0.60323	0.09517	0.67386	-0.0189
0.65041	0.0876	0.72497	-0.0118
0.69676	0.07903	0.77446	-0.0055
0.74171	0.0699	0.82144	-0.0004
0.78466	0.06055	0.86497	0.00324
0.82498	0.05125	0.90406	0.00526
0.86207	0.04221	0.93768	0.00567
0.89529	0.03348	0.96489	0.00463
0.92431	0.02493	0.98462	0.00262
0.94922	0.01669	0.99624	0.00073
0.96999	0.00946	1	0
0.98605	0.00405		
0.9964	0.00095		
1	0		